Monthly Notices of the ROYAL ASTRONOMICAL SOCIETY

MNRAS **503,** 3262–3278 (2021) doi:10.1093/mnras/stab465
Advance Access publication 2021 February 19

How are gamma-ray burst radio afterglows populated?

K. Zhang,[1,3] Z. B. Zhang,[1★] Y. F. Huang,[2★] L. M. Song,[3] S. J. Zheng,[3] X. J. Li,[1] D. Li [4,5★] and F. F. Su[1]

[1]*College of Physics and Engineering, Qufu Normal University, Qufu 273165, China*
[2]*School of Astronomy and Space Science, Nanjing University, Nanjing 210023, China*
[3]*Key Laboratory of Particle Astrophysics, Institute of High Energy Physics, Chinese Academy of Sciences, Beijing 100049, China*
[4]*National Astronomical Observatories of China, Chinese Academy of Sciences, 20A Datun Road, Beijing 100020, China*
[5]*NAOC-UKZN Computational Astrophysics Centre, University of KwaZulu-Natal, Durban 4000, South Africa*

Accepted 2021 February 11. Received 2021 January 7; in original form 2020 February 12

ABSTRACT

We systematically analyse two GRB samples with radio-loud and radio-quiet afterglows, respectively. It is interestingly found that the radio-selected GRB samples exhibit a clear dichotomy in terms of their distributions of intrinsic durations ($T_{\rm int}$), isotropic energies in γ-rays ($E_{\gamma,\rm iso}$), the circum-burst medium density (n), the spectral radio peak luminosity ($L_{\nu,p}$) and flux densities ($F_{\rm host}$) of host galaxies. On average, the values of $T_{\rm int}$, $E_{\gamma,\rm iso}$, n, $L_{\nu,p}$, and $F_{\rm host}$ of radio-quiet GRBs are relatively smaller than those of radio-loud ones. However, the redshifts and host flux densities of both samples are similarly distributed. In addition, a positive power-law correlation of $L_{\nu,p} \propto E_{\gamma,\rm iso}^{0.41\pm0.04}$ is found for the radio-loud sample, especially in accord with the supernova-associated GRBs, which is marginally consistent with that of the radio-quiet GRB sample. A negative correlation between $T_{\rm int}$ and z is confirmed to similarly hold for both radio-loud and radio-quiet GRBs. The dividing line between short and long GRBs in the rest frame is at $T_{\rm int} \simeq 1$ s. Consequently, we propose that the radio-selected GRBs could be originated from distinct progenitors and central engines, together with environments.

Key words: methods: data analysis – galaxies: general – radio continuum: ISM – radio continuum: transients – gamma-ray bursts – transients: supernovae.

1 INTRODUCTION

Gamma-ray bursts (GRBs) are instantaneous brightening event of gamma rays in the distant universe. After it was reported in 1973 (Klebesadel, Strong & Olson 1973), a lot of properties of progenitors have been investigated by many previously theoretical and observational researches, see review papers Piran (1999) and Zhang (2014) for details. Study of GRB afterglows is crucial to understand the central engine and the environment of distinct progenitors. The general interpretation is that a sudden energy release will produce a high temperature fireball expanding at a relativistic speed. The internal dissipation of the fireball leads to the gamma-rays, and the blast wave against the external medium produce the afterglow (Mészáros 2006; Rees & Meszaros 1992, 1994). The hydrodynamic evolution of the jetted outflows from the ultra-relativistic phase to the non-relativistic phase has been studied by a few authors (e.g. Huang, Dai & Lu 1999; Huang et al. 2003). But there are many questions remaining for GRBs, such as how the inner engine runs, the reason of flares in afterglow and so on (Paczynski 1990; Duncan & Thompson 1992; Woosley 1993; Mu et al. 2016; Hascoët et al. 2017; Becerra et al. 2019). As illustrated in Chandra & Frail (2012), the detecting rates of X-ray and optical afterglows are higher than that of radio afterglows. Due to the relatively longer time-scale of radio afterglows, one can have more opportunities to observe the radio afterglows in detail at a later period. In particular, the rebrightening phenomena of some radio afterglows caused by multiple activities of the inner engine of GRBs (Li et al. 2015), energy injection (Geng et al. 2018), supernova (SN) components, or the forward and reverse shock can be detected and utilized to constrain the above theoretical rebrightening models. At the same time, the statistical classifications of radio afterglows become more and more important and feasible with the data accumulation of the radio afterglows.

Chandra & Frail (2012) sorted 304 GRBs radio afterglows and found the detection rate to be about 31 per cent, that is obviously lower than those of X-ray and optical afterglows even after the *Swift* satellite was launched to detect more X-ray and optical afterglows than before. Also, they sorted radio afterglows at 8.5 GHz for detection and 3σ upper limit between 5 and 10 d and found that there was only little difference between them. The tiny difference was thought to be resulted from the telescope sensitivity (Chandra & Frail 2012). However, Hancock, Geansler & Murphy (2013) pointed out that the instrumental sensitivity was not the intrinsic reason for the difference mentioned above and they found that $60 \sim 70$ per cent of the radio-selected GRB samples are truly radio bright, while the convinced fraction of the radio faint GRBs is about one-third. Chandra & Frail (2012) found that there was an apparent correlation between the detectability and the energy of GRBs which may cause the diverse detection rates for the radio bright and faint GRB samples. To reduce the influence of many unknown reasons on classifications in terms of the radio brightness, Lloyd-Ronning & Fryer (2017) and Lloyd-Ronning et al. (2019) selected the GRBs with larger isotropic

★ E-mail: astrophy0817@163.com (ZBZ); hyf@nju.edu.cn (YFH); dili@nao.cas.cn (DL)

energy ($E_{\gamma,\,\rm iso} > 10^{52}$ erg) in prompt gamma-rays, and divided them into two sub-samples, that is radio-loud and radio-quiet types. They proposed that the two subsamples might be generated from different progenitors; that is the radio-loud GRBs might be produced from the He-merger while the radio-quiet GRBs may be interpreted by the core-collapse of massive stars.

Owing to the relatively less brightness of GRBs in radio bands, whether the radio afterglows can be classified into any subclasses is still controversial. With the increase of radio afterglow numbers, statistical study becomes more and more reliable and important. Motivated by the above incongruous results, we do a similar analysis but for different samples of GRB radio afterglows in very detail. In addition, we will examine the effects of surrounding mediums and GRB host galaxies on the GRB classifications in radio bands. In order to deduce their potential progenitors, several supernova-associated GRBs with radio afterglow measurements are also included. Simultaneously, we also pay attention to GW170817/GRB170817A detected by Laser Interferometer Gravitational-Wave Observatory (LIGO) and Fermi/Integral satellites (Goldstein et al. 2017; Savchenko et al. 2017) as the first short GRB associated with Kilonova originated from a binary neutron star merger system (Abbott et al. 2017).

2 DATA PREPARATION

First of all, we define our sampling criteria in the following: (1) GRBs with radio flux density at a signal-to-noise level of S/N ≥ 3 constitute the radio-loud sample; (2) those radio afterglows with a flux density at $1 <$ S/N < 3 levels belong to the radio-quiet (including upper limits) sample; and (3) other GRBs without any radio flux detections or with a lower level of S/N < 1 are regarded as a special radio-undetected sample. Note that each burst in the radio-undetected sample was indeed observed by some radio telescopes or arrays, but no meaningful flux densities were detected according to the literature (e.g. Chandra & Frail 2012) and the Gamma-ray Coordinates Network (GCN). Most probably, radio afterglows of the radio-undetected sample could exist but are too weak to be successfully detected by the current instruments due to sensitivity limits or influence of host galaxies (Zhang et al. 2018). Note that the fraction of the radio-undetected GRBs is roughly one fourth. In this study, we will not consider the radio-undetected sample and will only pay attention to comparisons between the radio-loud and the radio-quiet GRBs. We choose the GRBs with measured redshift (z) to calculate the intrinsic duration $T_{\rm int}$ and isotropic equivalent energy $E_{\gamma,\,\rm iso}$ (the intrinsic duration defined as $T_{\rm int} = T_{90}/(1+z)$, where T_{90} is defined as the time that the burst takes from 5 to 95 per cent counts of the total gamma-rays, Kouveliotou et al. 1993).

Chandra & Frail (2012) reported a large sample of GRB radio afterglows, of which the majority were detected by the Very Large Array (VLA) or Expanded Very Large Array (EVLA), and a small fraction of these radio afterglows were successfully observed by the Australia Telescope Compact Array (ATCA), Westerbork Synthesis Radio Telescope (WSRT), Giant Metrewave Radio Telescope (GMRT), and the Very Long Baseline Array (VLBA). Out of the 304 GRBs in Chandra & Frail (2012), we have selected 97 detections and 125 upper limits from the VLA-based afterglows, of which 79 radio-loud and 54 radio-quiet bursts with known redshift are involved (hereafter called the VLA-based sample). To compare with the recent high-frequency radio afterglows detected by the Arcminute Microkelvin Imager (AMI) telescope, we have taken 45 detections and 60 upper limits out of 139 bursts at 15.7 GHz from Anderson et al. (2018), from which 21 radio-loud and 23 radio-quiet AMI afterglows with measured redshift are picked out to study the rest-frame features (hereafter called the AMI sample). It is likely that the lower $E_{\gamma,\,\rm iso}$ bursts in the SN-associated GRB sample are relatively brighter in radio bands in contrast with other bursts. To explore the interesting issue, we have paid particular attention to the SN-associated GRBs and chosen 23 SN/GRBs as a unique subgroup including 21 radio-loud and 2 radio-quiet GRBs. It is noticeable that more than 90 per cent of SN/GRB afterglows are radio-loud and the redshifts of all the SN/GRBs in our sample are known and relatively lower than other GRBs (see Appendix A for details). Moreover, Lloyd-Ronning & Fryer (2017) and Lloyd-Ronning et al. (2019) only chose those energetic bursts with $E_{\gamma,\,\rm iso} > 10^{52}$ erg, which will inevitably bias the results of radio-quiet afterglows since the $E_{\gamma,\,\rm iso}$ and radio peak luminosity are positively correlated for different kinds of bursts as described in Section 3.6.

All the above samples of radio afterglows are compiled in Tables 1 and 2, in which, the key parameters of radio-loud and radio-quiet GRBs are similarly presented. Column 1 gives the name of GRBs; Columns 2 and 3 are the duration (T_{90}) and the redshift (z), respectively; In Column 4, we list the k-corrected isotropic energies ($E_{\gamma,\,\rm iso}$) in γ-ray band; Column 5 gives the medium densities n; Column 6 provides the spectral peak luminosity ($L_{\nu,\,p}$) of radio afterglows at a frequency of 8.5 or 15.7 GHz; In Columns 7 and 8, we present the peak radio flux density together 1σ RMS at 8.5 or 15.7 GHz; Column 9 lists the radio telescopes which were used to carry out observations; References are given in Column 10. If there is no any parameters measured, we just leave them blank. To investigate the properties of host galaxies for different kinds of radio samples, we directly utilize the data of radio flux densities for host galaxies in Li et al. (2015) and Zhang et al. (2018).

3 RESULTS

3.1 Flux density of radio afterglows

We first plot the distributions of radio afterglows for detections and 3σ upper limits between 0 and 10 d at 8.5 GHz in top left-hand panel of Fig. 1, where it is found that our distributions are similar to those in Chandra & Frail (2012) and Hancock et al. (2013), in which the upper limits are confirmed again to peak at 50–100 μJy in and the detections peaked around 200 μJy with a long extending tail. We also find that there is an obvious truncation at ~400 μJy in the VLA-based detection sample, which motivates us to examine whether the distribution of the flux densities less than 400 μJy is similar to that of the upper limit sample. For the purpose, we try to define the detection sample whose flux density larger than 400 μJy as radio-loud I sample, and other detections with radio flux density less than 400 μJy to be radio-loud II sample, temporally. It is interestingly found from the bottom panels of Fig. 1 that the flux density distributions of radio-loud and radio-quiet AMI afterglows are also bimodally distributed and resemble those of the VLA-based sample. However, the AMI peak flux densities of both detections and upper limits are on average two times larger than those VLA-based ones, correspondingly.

To check if it is necessary to reclassify radio-loud GRBs into two subsamples, we display the cumulative fractions of the intrinsic duration $T_{\rm int}$ and the $E_{\gamma,\,\rm iso}$ for radio-loud I, radio-loud II, and radio-quiet GRBs (upper limits) in Fig. 2. As shown in Table 4, the Kolmogorov–Smirnov (K-S) tests return the statistic $D = 0.37$ (0.27) and $P = 6 \times 10^{-3}$ (0.038) between the $T_{\rm int}$ distributions of the radio-loud I (II) and the radio-quiet samples, which indicates that the radio-quiet bursts are different from both radio-loud I and II ones.

Table 1. Physical parameters of radio-loud GRBs.

GRB	T_{90} (s)	z	$E_{\gamma,\,\mathrm{iso}}$ (erg)	n (cm^{-3})	$L_{\nu,\,p}$ (erg/s/Hz)	$f_{p,\,\mathrm{radio}}$ (uJy)	rms (uJy)	Radio telescope	Reference
970508	14	0.835	7.10E + 51	1	9.40E + 30	1270	33	VLA	1,4
970828	147	0.958	2.96E + 53	–	2.93E + 30	147	33	VLA	1
980329	58	2-3.9	2.10E + 54	20^{+10}_{-10}	4.76E + 31	465	16	VLA	1,5
980425⋆	31	0.009	1.60E + 48	–	8.56E + 28	49400	1000	ATCA	1
980519	30	–	–	$0.14^{+0.32}_{-0.03}$	1.95E + 31	1050	20	VLA	1,5
980703	90	0.966	6.90E + 52	28^{+10}_{-10}	1.95E + 31	1050	55	VLA	1,6
981226	20	1.11	5.90E + 51	–	4.40E + 30	169	28	VLA	1
990123	100	1.6	2.39E + 54	–	1.28E + 31	260	32	VLA	1
990506	220	1.307	9.49E + 53	–	2.02E + 31	581	45	VLA	1
990510	75	1.619	1.78E + 53	$0.29^{+0.11}_{-0.15}$	1.14E + 31	127	30	ATCA	1,7
991208⋆	60	0.706	1.10E + 53	18^{+18}_{-6}	2.23E + 31	1990	33	VLA	1,7
991216	25	1.02	6.75E + 53	$4.7^{+6.8}_{-1.8}$	2.14E + 31	960	67	VLA	1,7
000131	110	4.5	1.84E + 54	–	4.64E + 31	207	46	ATCA	1
000210	10	0.85	2.00E + 53	–	1.48E + 30	93	21	VLA	1
000301C	10	2.034	4.37E + 52	27^{+5}_{-5}	2.29E + 31	483	41	VLA	1
000418	30	1.119	7.51E + 52	27^{+250}_{-14}	2.26E + 31	1240	33	VLA	1,7
000911⋆	500	1.059	8.80E + 53	–	6.65E + 30	278	36	VLA	1
000926	25	2.039	2.70E + 53	27^{+3}_{-3}	4.84E + 31	666	60	VLA	1,7
001007	375	–	–	–	–	222	33	VLA	1
001018	31	–	–	–	–	405	50	VLA	1
010222	170	1.477	1.33E + 54	1.7	1.48E + 31	344	39	VLA	1,7
010921	24	0.45	9.00E + 51	–	1.06E + 30	229	22	VLA	1
011030	–	<3	–	–	2.26E + 31	219	20	VLA	1
011121	105	0.362	4.55E + 52	–	1.83E + 30	610	39	ATCA	1
011211	400	2.14	6.30E + 52	–	1.18E + 31	163	17	VLA	1
020305	247	–	–	–	–	76	15	VLA	1
020405⋆	40	0.69	1.10E + 53	8	5.22E + 30	487	34	VLA	1,5
020813	113	1.254	8.00E + 53	–	1.04E + 31	323	39	VLA	1
020819B	50	0.41	7.90E + 51	–	1.22E + 30	315	18	VLA	1
020903⋆	13	0.25	2.30E + 49	–	1.51E + 30	1058	19	VLA	1
021004	50	2.33	3.80E + 52	30^{+270}_{-27}	5.35E + 31	691	33	VLA	1,8
021206	20	–	–	–	–	1377	47	VLA	1
030115	36	2.5	3.91E + 52	–	9.34E + 30	94	22	VLA	1
030226	69	1.986	1.20E + 53	–	9.14E + 30	131	27	VLA	1
030323	20	3.372	3.39E + 52	–	4.28E + 30	530	170	VLA	1
030329⋆	63	0.169	1.80E + 52	1.8	1.01E + 31	19150	80	VLA	1,9
030723	31	–	–	–	–	219	22	VLA	1
031203⋆	30	0.105	1.15E + 50	0.6	1.34E + 29	811	40	VLA	1,10
040812	19	–	–	–	–	450	80	VLA	1
041219A	6	–	–	–	–	518	150	VLA	1
050315	96	1.95	5.70E + 52	–	2.03E + 31	300	62	VLA	1
050401	33	2.898	3.20E + 53	10	1.51E + 31	122	33	VLA	1,3
050416A⋆	3	0.65	1.00E + 51	3	4.12E + 30	431	46	VLA	1,3
050509C	25	–	–	–	–	404	58	VLA	1
050525A⋆	9	0.606	2.04E + 52	1.0×10^{-8}	1.37E + 30	178	46	VLA	1,3
050603	12	2.821	5.00E + 53	–	3.11E + 31	316	45	VLA	1
050713B	125	–	–	–	–	426	45	VLA	1
050724	96	0.258	9.00E + 49	0.1	7.08E + 29	465	29	VLA	1,11
050730	157	3.968	9.00E + 52	8	4.04E + 31	212	35	VLA	1,3
050820A	240	2.615	2.00E + 53	0.1	6.74E + 31	634	62	VLA	1,12
050824	23	0.83	1.50E + 51	1	2.32E + 30	152	34	VLA	1,3
050904	174	6.29	1.30E + 54	680	3.01E + 31	116	18	VLA	1,13
050922C	5	2.199	3.90E + 52	2	1.15E + 31	140	42	VLA	1,3
051022	200	0.809	6.30E + 53	–	8.49E + 30	585	49	VLA	1
051109A	37	2.346	2.30E + 52	–	1.06E + 31	117	24	VLA	1
051111	46	1.55	6.00E + 52	5.00×10^{-9}	4.56E + 30	98	28	VLA	1,3
051211B	80	–	–	–	–	68	19	VLA	1
051221A	1.4	0.547	2.80E + 51	0.001	6.01E + 29	88	26	VLA	1,14
060116	106	–	–	–	–	363	28	VLA	1
060218⋆	128	0.033	2.90E + 48	5	1.09E + 28	453	77	VLA	1,15
060418	103	1.49	1.00E + 53	10	9.41E + 30	216	48	VLA	1,3
061121	81	1.315	1.90E + 53	3	1.07E + 31	304	48	VLA	1,3

Table 1 – *continued*

GRB	T_{90} (s)	z	$E_{\gamma,\,\mathrm{iso}}$ (erg)	n (cm^{-3})	$L_{\nu,\,p}$ (erg/s/Hz)	$f_{p,\,\mathrm{radio}}$ (uJy)	rms (uJy)	Radio telescope	Reference
061222A	72	2.088	1.03E + 53	–	2.15E + 31	285	68	VLA	1
070125	60	1.548	9.55E + 53	42	2.61E + 31	660	39	VLA	1,16
070612A	369	0.617	9.12E + 51	–	5.09E + 30	589	54	VLA	1
071003	148	1.604	3.24E + 53	–	2.12E + 31	431	51	VLA	1
071010B	36	0.947	2.60E + 52	–	6.43E + 30	330	52	VLA	1
071020	4	2.146	8.91E + 52	–	1.47E + 31	186	22	VLA	1
071021	229	<5.6	–	–	4.39E + 31	149	44	VLA	1
071109	30	–	–	–	–	188	42	VLA	1
071122	80	1.14	3.47E + 51	–	6.96E + 30	255	45	VLA	1
080229	64	–	–	–	–	635	44	VLA	1
080319*B*⋆	125	0.937	1.45E + 54	10	4.43E + 30	232	42	VLA	1,3
080603A	150	1.687	–	–	1.23E + 31	230	29	VLA	1
080810	108	3.35	5.37E + 53	–	2.29E + 31	151	50	VLA	1
081203B	23	–	–	–	–	162	44	VLA	1
081221	34	–	–	–	–	167	27	VLA	1
090313	71	3.375	4.57E + 52	0.6	8.81E + 31	576	44	VLA	1
090323	133	3.57	4.10E + 54	0.1	3.72E + 31	225	35	VLA	1,17
090328	57	0.736	1.00E + 53	0.26	9.81E + 30	809	39	VLA	1,17
090418	56	1.608	2.57E + 53	–	1.08E + 31	219	44	VLA	1
090423	10	8.26	1.10E + 53	0.9	4.63E + 31	92.4	22.7	VLA	1,18
090424	50	0.544	4.47E + 52	–	4.54E + 30	673	39	VLA	1
090618⋆	113	0.54	2.21E + 53	–	3.67E + 30	551	51	VLA	1
090709A	89	<6.1	–	–	5.68E + 31	174	53	VLA	1
090715B	265	3	2.36E + 53	–	3.33E + 31	257	57	VLA	1
090902B	–	1.883	3.09E + 54	–	8.33E + 30	130	34	VLA	1
091020	39	1.71	4.56E + 52	–	2.47E + 31	451	44	VLA	1
100413A	191	<3.5	–	–	2.56E + 31	159	15	EVLA	1
100414A	26	1.368	7.79E + 53	–	1.56E + 31	415	15	EVLA	1
100418A⋆	7	0.62	5.20E + 50	–	3.99E + 30	458	22	EVLA	1
100805A	15	–	–	–	–	108	32	EVLA	1
100814A	175	1.44	5.97E + 52	–	1.90E + 31	462	25	EVLA	1
100901A	439	1.408	1.78E + 52	–	1.74E + 31	440	27	EVLA	1
100906A	114	1.727	1.34E + 53	–	1.20E + 31	215	28	EVLA	1
101219B⋆	34	0.552	2.96E + 52	–	4.93E + 29	71	15	EVLA	1
110428A	5.6	–	–	–	–	69	18	EVLA	1
120320A	25.74	–	–	–	–	380	80	AMI	19,20
120326A	69.6	1.798	3.82E + 52	–	5.12E + 31	860	80	AMI	19,20
120514A	164.4	–	–	–	–	460	130	AMI	19,20
121031A	62.5	0.1126	–	–	1.91E + 29	670	220	AMI	19,20
121128A	23	2.2	8.20E + 52	–	2.62E + 31	320	90	AMI	19,20
130216A	6.5	–	–	–	–	990	100	AMI	19,20
130427A⋆	162.83	0.338	8.50E + 53	–	1.19E + 31	4540	80	AMI	19,20
130419A	75.7	–	–	–	–	1700	120	AMI	19,20
130508A	42	–	–	–	–	550	140	AMI	19,20
130603A	–	–	–	–	–	470	130	AMI	19,20
130604A	37.7	1.06	–	–	9.34E + 30	390	70	AMI	19,20
130606A	276.58	5.91	2.83E + 53	–	8.17E + 31	260	70	AMI	19,20
130608A	44.4	–	–	–	–	240	80	AMI	19,20
130612A	110	2.006	7.19E + 51	–	2.34E + 31	330	90	AMI	19,20
130625A	38.1	–	–	–	–	590	110	AMI	19,20
130702A⋆	59	0.145	6.36E + 50	–	7.42E + 29	1560	130	AMI	19,20
130907A	115	1.238	3.30E + 54	–	3.29E + 31	1040	100	AMI	19,25,20
131024B	64	–	–	–	–	610	70	AMI	19,20
140108A	97.8	0.6	4.00E + 52	–	3.03E + 30	370	50	AMI	19,20
140209A	21.3	–	–	–	–	430	90	AMI	19,20
140215A	84.2	–	–	–	–	240	50	AMI	19,20
140304A	32	5.28	1.03E + 53	–	1.04E + 32	380	40	AMI	19,20
140305A	13.7	–	–	–	–	420	40	AMI	19,20
140318A	8.43	1.02	–	–	6.25E + 30	280	40	AMI	19,20
140320B	–	–	–	–	–	470	30	AMI	19,20
140320C	–	–	–	–	–	140	40	AMI	19,20
140423A	134	3.26	4.38E + 53	–	3.35E + 31	230	70	AMI	19,20
140430A	173.6	1.6	–	–	1.37E + 32	2800	110	AMI	19,20

Table 1 – *continued*

GRB	T_{90} (s)	z	$E_{\gamma,\,\rm iso}$ (erg)	n ($\rm cm^{-3}$)	$L_{\nu,\,p}$ (erg/s/Hz)	$f_{p,\,\rm radio}$ (uJy)	rms (uJy)	Radio telescope	Reference
140606A	0.34	–	–	–	–	530	50	AMI	19,20
140606B	23.6	0.384	2.50E + 51	–	1.69E + 29	50	60	AMI	19,20
140607A	109.9	–	–	–	–	590	80	AMI	19,20
140629A	42	2.275	4.40E + 52	–	1.29E + 31	150	50	AMI	19,20
140703A	84	3.14	1.84E + 53	–	6.78E + 31	490	60	AMI	19,20
140709A	98.6	–	–	–	–	460	40	AMI	19,20
140713A	5.3	–	–	–	–	1370	40	AMI	19,20
140903A	0.3	0.351	4.40E + 49	–	2.04E + 30	720	70	AMI	19,20
141015A	11	–	–	–	–	280	60	AMI	19,20
141020A	15.55	–	–	–	–	300	60	AMI	19,20
141109B	54.2	–	–	–	–	910	250	AMI	19,20
141121A	549	1.47	8.00E + 52	–	1.57E + 31	370	40	AMI	19,20
141212A	0.3	0.596	6.80E + 49	–	1.37E + 30	170	40	AMI	19,20
141212B	10.5	–	–	–	–	110	30	AMI	19,20
150110B	10.6	–	–	–	–	530	40	AMI	19,20
150413A	263.6	3.139	6.53E + 53	–	3.18E + 31	230	40	AMI	19,20
150213B	181	–	–	–	–	140	40	AMI	19,20
161219B⋆	6.94	0.1475	1.16E + 50		1.37E + 29	278.1	28.6	VLA	19,21
171205A⋆	189.4	0.0368	2.18E + 49		1.71E + 29	5710	50	VLA	19,22
180720B⋆	49	0.654	3.40E + 53		1.06E + 31	1096	62	AMI	19,23
190114C⋆	361.5	0.42	2.40E + 53		2.46E + 30	607	17.3	VLA	19,23
190829A⋆	58.2	0.0785	2.00E + 50		5.36E + 29	3889	197	AMI	19,24

Note. In Column 1, symbol ⋆ represents the SN/GRB. References are given in order for duration time (T_{90}), redshift(z), isotropic equivalent energy($E_{\gamma,\,\rm iso}$), peak flux density($f_{p,\,\rm radio}$), and medium density(n), repectively. [1] Chandra & Frail (2012); [2] Friedman & Bloom (2005); [3] Ghisellini et al. (2009); [4] Frail, Waxman & Kulkarni (2000); [5] Bloom et al. (2003); [6] Frail et al. (2003); [7] Panaitescu & Kumar (2002); [8] Schaefer et al. (2003); [9] Berger et al. (2003); [10] Soderberg et al. (2004); [11] Berger et al. (2005); [12] Cenko et al. (2006); [13] Frail et al. (2006); [14] Soderberg et al. (2006a); [15] Soderberg et al. (2006b); [16] Chandra et al. (2008); [17] Cenko et al. (2011); [18] Chandra et al. (2010); [19] https://gcn.gsfc.nasa.gov/gcn3_archive.html; [20] Anderson et al. (2018); [21] Laskar et al. (2018); [22] Urata et al. (2019); [23] Rhodes (et al.); [24] Laskar et al. (2020); [25] Veres et al. (2015)

Similarly, the statistic and p-value of the $E_{\gamma,\,\rm iso}$ distributions are $D = 0.32$ (0.45) and $P = 0.03$ (9.2×10^{-5}) for comparisons between the radio-quiet and the radio-loud I (II) samples. Surprisingly, the K-S test to the radio-loud I and the radio-loud II samples returns $D = 0.27$ with $P = 0.24$ for the $T_{\rm int}$ distribution and $D = 0.14$ with $P = 0.92$ for the $E_{\gamma,\,\rm iso}$ distribution, indicating that the two radio-loud sub-samples should be taken from the same parent distribution. In other words, dividing radio-loud bursts into two classes is not necessary. Consequently, we shall only investigate the radio-loud and the radio-quiet samples in the subsequent sections, and explore in statistics whether they are basically different kinds of bursts on basis of their observational properties.

3.2 Distributions of z, $T_{\rm int}$, and $E_{\gamma,\,\rm iso}$ revisited

Using the total sample of 177 GRBs including 133 VLA-based and 44 AMI bursts, we plot the histograms of z, $E_{\gamma,\,\rm iso}$, and $T_{\rm int}$ for radio-loud and radio-quiet samples in Fig. A1, where one can find that the distributions of z, $T_{\rm int}$, and $E_{\gamma,\,\rm iso}$ of radio-loud and radio-quiet samples are well fitted by a Gaussian function. The fitting results are summarized in Table 3, from which we notice that the mean values of $E_{\gamma,\,\rm iso}$ and $T_{\rm int}$ of radio-quiet GRBs are systematically smaller than radio-loud burst samples. Surprisingly, the averaged redshifts of radio-quiet and radio-loud GRBs are quite similar in statistics.

Following Hancock et al. (2013) and Lloyd-Ronning et al. (2019), we also analyse the cumulative fractions of the $T_{\rm int}$ and the $E_{\gamma,\,\rm iso}$ but for different radio-loud and radio-quiet VLA-based samples in Fig. 3 and Table 4, where we see that the radio-quiet samples are evidently different from the radio-loud ones in terms of the $T_{\rm int}$ distribution, on average the radio-loud GRBs have relatively longer $T_{\rm int}$ as found before (Hancock et al. 2013; Lloyd-Ronning et al. 2019). Regarding the $E_{\gamma,\,\rm iso}$ distributions, we also perform the K-S tests to the two VLA-based samples and find from Table 4 that they are drawn from different parent distributions.

With the increase of frequency, it is interestingly found that two AMI samples of radio-loud and radio-quiet GRBs at 15.7 GHz are consistent with being drawn from the same parent $E_{\gamma,\,\rm iso}$ distribution.

3.3 Radio fluxes of host galaxies

We notice that some GRBs with radio flux densities of host galaxies in Zhang et al. (2018) were not included in our initial radio-loud or radio-quiet samples. To increase the reliability in statistics, we assume them to be radio-undetected or radio-quiet because they do not have radio afterglows detected. In order to analyse the radio flux density of host galaxies, we combine the data of radio-undetected and radio-quiet into a simple radio-faint sample. Then, we plot the cumulative fractions for the radio-loud and radio-faint samples in Fig. 4 where we find when the radio (flux density of the host galaxies, $F_{\rm host}$) is less than 50 μJy the radio-loud, the radio-faint samples share the same distribution, but when it is more than 50 μJy, the cumulative fractions of these two samples are significantly different. A K-S test shows that the probability of those two samples from the same distribution is 0.19, so that in terms of host galaxies the two samples might be taken from the same distribution.

Li et al. (2015) found the host flux density $F_{\rm host}$ is positively correlated with the observed peak flux density ($F_{o,\,\rm peak}$) or the pure

Table 2. Physical parameters of radio-quiet GRBs.

GRB	T_{90} (*s*)	z	$E_{\gamma,\,\mathrm{iso}}$ (erg)	n (cm^{-3})	$L_{\nu,\,p}$ (erg/s/Hz)	$f_{p,\,\mathrm{radio}}$ (uJy)	rms (uJy)	Radio telescope	Reference
970228⋆	56	0.695	1.60E + 52	–	8.26E + 29	76	50	VLA	1
971214	35	3.42	2.11E + 53	–	1.14E + 31	73	50	VLA	1
990217	–	–	–	–	–	<280	56	ATCA	1,8
990712	30	0.433	6.72E + 51	–	2.58E + 29	60	50	ATCA	1
991014	3	–	–	–	–	<125	25	VLA	1,8
000214	115	0.47	8.00E + 51	–	1.19E + 30	<235	59	ATCA	1,8
000326	2	–	–	–	–	<124	62	VLA	1,8
000528	80	–	–	–	–	<140	47	VLA	1,8
000607	0.2	–	–	–	–	<370	74	VLA	1,8
000615A	12	–	–	–	–	<150	50	VLA	1,8
000630	20	–	–	–	–	70	62	VLA	1
000801	30	–	–	–	–	<200	50	VLA	1,8
001025B	0.3	–	–	–	–	<700	140	VLA	1,8
001204	0.5	–	–	–	–	<250	50	VLA	1,8
010119	0.2	–	–	–	–	<350	70	VLA	1,8
010214	15	–	–	–	–	<210	42	VLA	1,8
020124	41	3.2	3.00E + 53	3	1.19E + 31	84	30	VLA	1,7
020127	26	1.9	3.57E + 52	–	1.02E + 31	<157	43	VLA	1,8
020321	70	–	–	–	–	<114	38	ATCA	1
020322	75	–	–	–	–	<125	35	VLA	1,8
020410	1800	–	–	–	–	64	51	ATCA	1
020427	66	–	–	–	–	<70	35	ATCA	1,8
020531	1	1	–	–	3.88E + 30	<180	60	VLA	1,8
021008	30	–	–	–	–	<175	35	VLA	1,8
021125	25	–	–	–	–	<220	44	VLA	1,8
021201	0.3	–	–	–	–	<500	150	VLA	1,8
021211⋆	8	1.01	1.10E + 52	–	1.32E + 30	60	28	VLA	1
021219	6	–	–	–	–	<220	55	VLA	1,8
030227	33	–	–	–	–	64	24	VLA	1
030324	16	–	–	–	–	<180	60	VLA	1,8
030418	110	–	–	–	–	69	27	VLA	1
030429	25	2.658	2.19E + 52	–	9.14E + 30	84	54	VLA	1
030528	84	0.782	3.04E + 52	–	4.74E + 30	<350	70	VLA	1,8
031111	10	–	–	–	–	<77	77	VLA	1,8
040223	258	–	–	–	–	<174	100	VLA	1,8
040701	60	0.21	8.02E + 49	–	–	$<2\sigma$	–	VLA	1,8
040827	49	–	–	–	–	<700	35	VLA	1,8
040912	127	1.563	1.65E + 51	–	5.65E + 30	<120	40	VLA	1,8
040916	450	–	–	–	–	<99	33	VLA	1,8
040924	5	0.859	1.10E + 52	–	2.39E + 30	<147	49	VLA	1,8
041006	25	0.716	3.50E + 52	–	9.44E + 29	<82	59	VLA	1,8
041218	60	–	–	–	–	<70	25	VLA	1,8
050117A	167	–	–	–	–	<56	28	VLA	1,8
050124	4	–	–	–	–	<99	50	VLA	1,8
050126	25	1.29	8.00E + 51	–	4.59E + 30	<135	45	VLA	1,8
050128	19	–	–	–	–	<150	31	VLA	1,8
050202	0.3	–	–	–	–	$<5\sigma$	–	VLA	1,8
050306	158	–	–	–	–	56	28	VLA	1
050319	153	3.24	4.60E + 52	1.00E–08	1.92E + 31	<133	67	VLA	1,10,8
050408	15	1.236	3.44E + 52	0.01	1.58E + 29	<78	39	VLA	1,6
050410	43	–	–	–	–	<114	57	VLA	1,8
050412	27	–	–	–	–	<38	19	VLA	1,8
050421	15	–	–	–	–	<34	27	VLA	1,8
050509B	0.07	0.225	2.40E + 48	–	4.39E + 28	38	22	VLA	1
050520	80	–	–	–	–	<57.6	29	VLA	1,8
050522	15	–	–	–	–	<153	51	VLA	1,8
050607	26	–	–	–	–	59	23	VLA	1
050709	0.07	0.161	1.00E + 51	$1^{+0.5}_{-0.4}$		$<5\sigma$	–	VLA	1,2,8
050712	52	–	–	–	–	<96	55	VLA	1,8
050714B	54	–	–	–	–	<102	51	VLA	1,8
050803	88	–	–	–	–	<102	54	VLA	1,8
050813	0.5	0.72	1.50E + 50	–	6.40E + 29	<55	36	VLA	1,8
050906	0.3	–	–	–	–	<61	45	VLA	1,8
050801	19	1.38	3.24E + 51	1.00×10^{-8}	5.31E + 30	139	50	VLA	1,5
050814	151	5.3	6.00E + 52	–	2.01E + 31	73	36	VLA	1
050815	3	–	–	–	–	77	45	VLA	1
050915A	52	–	–	–	–	43	31	VLA	1
051008	280	–	–	–	–	<80	40	VLA	1,8
051016B	4	0.936	3.70E + 50	–	6.67E + 29	35	13	VLA	1
051021A	27	–	–	–	–	36	25	VLA	1
051105A	0.09	–	–	–	–	$<5\sigma$	–	VLA	1,8

Table 2 – *continued*

GRB	T_{90} (*s*)	z	$E_{\gamma,\,\mathrm{iso}}$ (erg)	n (cm^{-3})	$L_{\nu,\,p}$ (erg/s/Hz)	$f_{p,\,\mathrm{radio}}$ (uJy)	rms (uJy)	Radio telescope	Reference
051109B	14	0.08	3.60E + 48	–	3.58E + 27	25	23	VLA	1
051114	–	–	–	–	–	$<4\sigma$	–	VLA	1,8
051117A	136	–	–	–	–	$<3\sigma$	–	VLA	1,8
051117B	9	–	–	–	–	$<3\sigma$	–	VLA	1,8
060105	54	–	–	3	–	49	47	VLA	1,4
060123	900	1.099	–	–		$<4\sigma$	–	VLA	1,8
060206	8	4.05	4.07E + 52	2	7.63E + 30	39	22	VLA	1,10
060210	255	3.91	4.20E + 53	1.00E–08		$<3\sigma$	–	VLA	1,10,8
060313	0.7	–	–	$0.0033^{+1}_{-0.5}$	–	$<3\sigma$	–	VLA	1,2,8
060522	71	5.11	7.00E + 52	–	1.00E + 31	38	17	VLA	1
060604	95	2.68	4.37E + 51	–	1.43E + 31	130	65	VLA	1
060605	79	3.773	2.50E + 52	–	1.67E + 31	94	47	VLA	1
060707	66	3.43	6.10E + 52	–	1.28E + 31	82	41	VLA	1
060719	67	<4.6	–	–	4.15E + 31	180	60	ATCA	1
060801	0.5	1.131	3.09E + 51	–	2.83E + 30	105	35	VLA	1
060825	8	–	–	–	–	94	47	VLA	1
060908	19	1.884	7.00E + 52	10	3.27E + 30	51	26	VLA	1,5
060912A	5	0.937	8.00E + 51	–	1.24E + 30	65	32	VLA	1
060923A	52	–	–	–	–	110	55	VLA	1
060923C	76	–	–	–	–	100	50	VLA	1
060926	8	3.209	1.00E + 52	–	1.34E + 31	94	56	VLA	1
061028	106	0.76	2.29E + 51	–	1.03E + 30	80	40	VLA	1
061210	85	0.41	9.00E + 50	–	2.62E + 29	68	34	VLA	1
070306	210	1.497	6.00E + 52	–	2.63E + 30	<60	30	VLA	1,8
070518	5.5	–	–	–	–	<64	32	VLA	1,8
070714B	3	0.923	1.10E + 52	$0.056^{+0.024}_{-0.011}$	1.67E + 30	<48	45	VLA	1,2
070724	0.4	0.457	2.45E + 49	1.90×10^{-5}		$<3\sigma$	–	VLA	1,2,8
070724B	50	–	–	–	–	<47	36	VLA	1
070729	0.9	–	–	–	–	<99	85	VLA	1
070923	0.2	–	–	–	–	<90	35	VLA	1,8
071010A	6	0.985	1.32E + 51	3	1.47E + 30	<66	35	VLA	1,5
071011	81	–	–	–	–	<106	60	VLA	1
071112B	0.3	–	–	–	–	$<5\sigma$	–	VLA	1,8
071112C	15	0.823	1.95E + 52	–	1.14E + 30	<57	38	VLA	1
080120	15	–	–	–	–	$<2\sigma$	–	VLA	1,8
080212	117	–	–	–	–	83	51	VLA	1
080413B	8	1.101	1.59E + 52	–	2.21E + 30	86	36	VLA	1
080430	14	0.767	3.00E + 51	–	8.92E + 29	68	46	VLA	1
080604	69	1.417	7.08E + 51	–	3.12E + 30	<70	39	VLA	1
080702A	0.5	–	–	–	–	<82	52	VLA	1
080721	176	2.591	1.23E + 54	–	9.75E + 30	93	48	VLA	1
080723B	95	–	–	–	–	<170	67	ATCA	1,8
080913	8	6.733	6.46E + 52	–	4.07E + 31	111	51	VLA	1
081203A	223	2.05	3.47E + 53	–	5.57E + 30	76	54	VLA	1
081222	33	2.77	3.54E + 53	–	6.24E + 30	54	53	VLA	1
090102	29	1.547	1.99E + 53	–	4.22E + 30	91	49	VLA	1
090417A	0.07	–	–	–	–	<104	35	VLA	1,8
090417B	283	0.345	1.10E + 51	–	3.28E + 29	<120	40	VLA	1,8
090429B	5.5	9.4	5.56E + 52	–	2.93E + 31	55	37	VLA	1
090812	75	2.452	4.40E + 53	–	5.99E + 30	104	43	VLA	1
100420	48	<20	–	–	–	24	17	EVLA	1
100424A	104	2.465	–	–	6.42E + 30	<66	22	EVLA	1,8
100528A	25	–	–	–	–	<48	46	EVLA	1
101112A	35	–	–	–	–	149	54	EVLA	1
120305A	0.1	–	–	–	–	260 ± 90	110	AMI	8,9
120311A	3.5	–	–	–	–	210 ± 80	80	AMI	8,9
120324A	118	–	–	–	–	110 ± 70	90	AMI	8,9
120308A	60.6	–	–	–	–	80 ± 50	60	AMI	8,9
120403A	1.25	–	–	–	–	190 ± 100	90	AMI	8,9
120404A	38.7	2.876	–	–	6.71E + 31	330 ± 1090	100	AMI	8,9
120521C	26.7	–	–	–	–	150 ± 250	130	AMI	8,9
120711B	60	–	–	–	–	230 ± 60	80	AMI	8,9
120722A	42.4	–	–	–	–	670 ± 1090	510	AMI	8,9
120729A	71.5	0.8	2.30E + 52	–	2.56E + 30	180 ± 100	100	AMI	8,9
120803B	37.5	–	–	–	–	210 ± 110	120	AMI	8,9
120805A	48	–	–	–	–	370 ± 140	170	AMI	8,9
120816A	7.6	–	–	–	–	440 ± 730	190	AMI	8,9
120911A	17.8	–	–	–	–	100 ± 50	90	AMI	8,9
120913A	30.1	–	–	–	–	160 ± 80	70	AMI	8,9
120927A	43	–	–	–	–	210 ± 100	160	AMI	8,9
121011A	75.6	–	–	–	–	190 ± 100	150	AMI	8,9

Table 2 – *continued*

GRB	T_{90} (s)	z	$E_{\gamma,\,\rm iso}$ (erg)	n ($\rm cm^{-3}$)	$L_{\nu,\,p}$ (erg/s/Hz)	$f_{p,\,\rm radio}$ (uJy)	rms (uJy)	Radio telescope	Reference
121017A	4.2	–	–	–	–	310 ± 870	150	AMI	8,9
121125A	52.2	–	–	–	–	370 ± 150	170	AMI	8,9
121202A	17.7	–	–	–	–	550 ± 240	290	AMI	8,9
130102A	77.5	–	–	–	–	110 ± 220	60	AMI	8,9
130131B	4.3	2.539	–	–	1.02E + 31	200 ± 360	160	AMI	8,9
130418A	300	1.218	6.30E + 52	–	2.76E + 30	180 ± 100	130	AMI	8,9
130420A	123.5	1.297	6.20E + 52	–	2.74E + 30	160 ± 100	120	AMI	8,9
130420B	10.2	–	–	–	–	260 ± 90	100	AMI	8,9
130502A	3	–	–	–	–	300 ± 180	180	AMI	8,9
130511A	5.43	1.3	–	–	2.69E + 31	780 ± 1800	390	AMI	8,9
130521A	11	–	–	–	–	220 ± 520	110	AMI	8,9
130603B	0.18	0.356	2.10E + 51	–	6.11E + 29	90 ± 50	60	AMI	8,9
130610A	46.4	2.092	5.78E + 52	–	1.06E + 31	140 ± 70	100	AMI	8,9
130701A	4.38	1.155	2.10E + 52	–	4.75E + 30	170 ± 70	70	AMI	8,9
130806A	–	–	–	–	–	640 ± 2470	150	AMI	8,9
130831A	32.5	0.479	4.60E + 51	–	1.37E + 30	120 ± 70	70	AMI	8,9
131002A	55.59	–	–	–	–	170 ± 80	90	AMI	8,9
140103A	17.3	–	–	–	–	50 ± 70	40	AMI	8,9
140114A	139.7	–	–	–	–	90 ± 60	60	AMI	8,9
140129B	1.36	1.5	–	–	6.17E + 30	50 ± 30	40	AMI	8,9
140206A	93.6	2.74	2.78E + 54	–	2.96E + 31	180 ± 80	90	AMI	8,9
140211A	89.4	–	–	–	–	100 ± 30	40	AMI	8,9
140419A	94.7	3.956	1.90E + 52	–	3.98E + 31	100 ± 50	60	AMI	8,9
140428A	17.42	4.7	–	–	2.61E + 31	100 ± 40	40	AMI	8,9
140502A	16.9	–	–	–	–	500 ± 1750	60	AMI	8,9
140508A	44.3	1.03	2.10E + 53	–	2.50E + 30	80 ± 40	50	AMI	8,9
140515A	23.4	6.32	5.38E + 52	–	1.57E + 32	460 ± 960	120	AMI	8,9
140516A	0.19	–	–	–	–	170 ± 90	70	AMI	8,9
140518A	60.5	4.707	5.98E + 52	–	4.51E + 31	80 ± 40	40	AMI	8,9
140521A	9.88	–	–	–	–	120 ± 90	40	AMI	8,9
140623A	–	–	–	–	–	140 ± 40	50	AMI	8,9
140710A	3.52	0.558	–	–	5.68E + 29	80 ± 50	70	AMI	8,9
140801A	7	1.32	4.90E + 52	–	4.51E + 31	140 ± 50	50	AMI	8,9
140907A	79.2	1.21	2.71E + 52	–	2.12E + 30	140 ± 100	110	AMI	8,9
141005A	4.34	–	–	–	–	270 ± 900	70	AMI	8,9
141026A	146	3.35	–	–	5.60E + 31	70 ± 40	40	AMI	8,9
141031B	16	–	–	–	–	50 ± 30	40	AMI	8,9
150120A	1.2	0.46	1.90E + 50	–	8.73E + 29	50 ± 30	40	AMI	8,9
150211A	13.6	–	–	–	–	80 ± 40	50	AMI	8,9
150212A	11.4	–	–	–	–	370 ± 1810	40	AMI	8,9
150309A	242	–	–	–	–	70 ± 30	40	AMI	8,9
150314A	14.79	1.758	6.70E + 53	–	9.17E + 30	110 ± 60	70	AMI	8,9
150317A	23.29	–	–	–	–	80 ± 40	40	AMI	8,9

Note. In Column 1, symbol ⋆ represents the SN/GRB. The peak flux density in Column 7 is the upper limit or less than 3σ. References are given in order for duration time (T_{90}), redshift (z), isotropic equivalent energy ($E_{\gamma,\,\rm iso}$), and medium density(n), respectively. [1] Chandra & Frail (2012); [2] Fong et al. (2015); [3] Cusumano et al. (2007); [4] Tashiro et al. (2007); [5] Ghisellini et al. (2009);[6] de Ugarte Postigo et al. (2007); [7] Bloom et al. (2003); [8] https://gcn.gsfc.nasa.gov/gcn3_archive.html; [9] Anderson et al. (2018); [10] Ghisellini et al. (2009)

flux density($F_{b,\,\rm peak}$) of GRBs at a given radio frequency ν as follows

$$F_{\rm host} = (a + b\nu)F_{o,\rm peak}, \tag{1}$$

and

$$F_{\rm host} = \frac{a + b\nu}{1 - (a + b\nu)}F_{b,\rm peak}, \tag{2}$$

where $a \simeq 0.3$, $b \simeq -0.02$, and $F_{o,\,\rm peak} = F_{b,\,\rm peak} + F_{\rm host}$. The equation (1) can be used to estimate the host flux density once the peak values of radio afterglows are measured. Fig. 5 displays the relationships of $F_{\rm host}$ with $F_{o,\,\rm peak}$ or $F_{b,\,\rm peak}$ for the radio-loud and radio-quiet samples. One can find that the radio flux densities of the radio-quiet GRBs and their host galaxies are relatively lower than those of the radio-loud ones. It is noticeable that the very famous nearby short GRB (sGRB) 170817A seen off-axis with an estimated viewing angle of $20^\circ \sim 40^\circ$ (Alexander et al. 2017) is the first electromagnetic counterpart of gravitational-wave event. It has peak flux densities of ∼84.5 and ∼58.6 μJy observed correspondingly at ν =3 and 5.5 GHz around 130 d since the merge of double neutron stars (Li et al. 2018). Using the above equation (1) and (2), one can easily predict the host flux densities to be about 20.3 μJy at $\nu = 3$ GHz and 11.1 μJy at $\nu = 5.5$ GHz. Interestingly, GW 170817/sGRB170817A as a radio-loud burst has relatively weaker radio afterglows and lower host fluxes in contrast with other normal radio-loud GRBs. However, it is located near the radio-quiet bursts as shown in Fig. 5, which indicates that galactic types or circum-burst environment of different radio-selected GRBs could be diverse although their dominant radiation mechanisms might be the same.

3.4 The surrounding medium density

As pointed out by Chandra & Frail (2012), the centimeter radio afterglow emission is the brightest for circum-burst densities from 1 to 10 $\rm cm^{-3}$. Beyond the narrow density range, the flux density will become weak due to either a low intrinsic emission strength (for lower

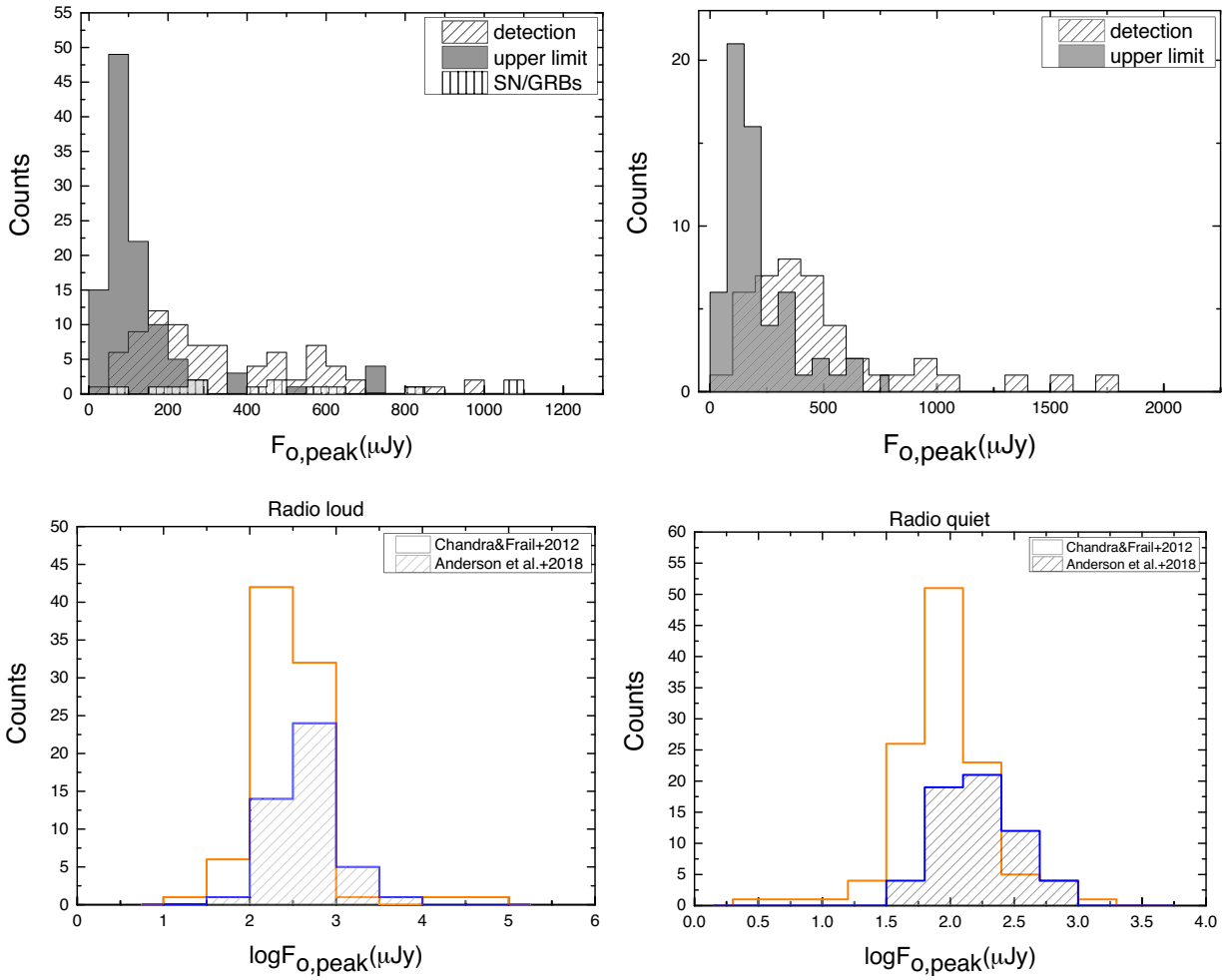

Figure 1. The distributions of peak flux densities for detections and upper limits of radio-loud (filled) and radio-quiet (hatched) afterglows between 0 and 10 d taken from Chandra & Frail (2012) at 8.5 GHz and Anderson et al. (2018) at 15.7 GHz are shown on the top left- and right-hand panels, respectively. The vertical shadow on the top left-hand panel represents the distributional histogram of SN/GRBs. Two bottom panels display the peak flux comparisons of radio afterglows at different frequencies for radio-loud (left-hand panels) and radio-quiet (right-hand panels) samples in the logarithmic scale.

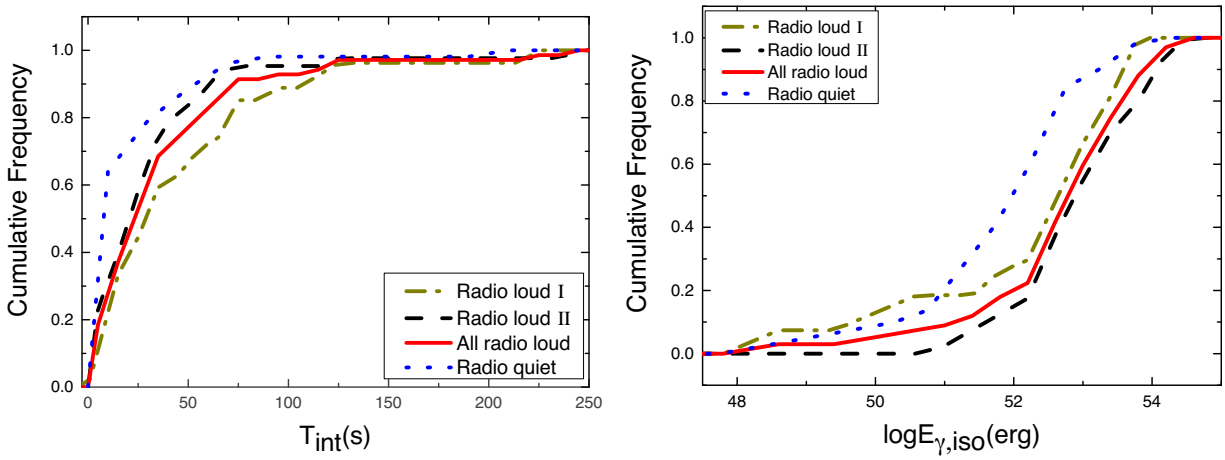

Figure 2. The cumulative fractions of $T_{\rm int}$ and $E_{\gamma,\,\rm iso}$ are shown for different radio-selected GRBs in left- and right-hand panels, respectively.

densities) or the increased synchrotron self-absorption (for higher densities). From the literatures, it is well known that the circum-burst medium densities (n) of GRBs usually span serval orders of magnitude and are hard to be determined (e.g. Wijers & Galama 1999; Chandra & Frail 2012; Fong et al. 2015; Zhang et al. 2018). In our samples, the circum-burst densities are distributed in a fairly wide scope spanning ∼10 orders of magnitude seen from Table 1 to 2. Because the number of radio-undetected GRBs with estimated

Table 3. Statistical parameters of the distributions of z, $T_{\rm int}$, and $E_{\gamma,\,\rm iso}$.

Sample	$\langle \log z \rangle$	$\sigma_{\log z}$	χ^2/dof	$\langle \log E_{\gamma,\,\rm iso} \rangle$	$\sigma_{\log E_{\gamma,\,\rm iso}}$	χ^2/dof	$\langle \log T_{\rm int} \rangle$	$\sigma_{\log T_{\rm int}}$	χ^2/dof
Radio-loud($N = 100$)	0.18 ± 0.01	0.69 ± 0.03	1.84	53.00 ± 0.04	1.80 ± 0.09	1.94	1.48 ± 0.02	0.86 ± 0.04	1.72
Radio-quiet($N = 77$)	0.19 ± 0.01	0.90 ± 0.03	0.91	52.35 ± 0.03	1.43 ± 0.06	1.36	0.98 ± 0.04	1.73 ± 0.09	1.98

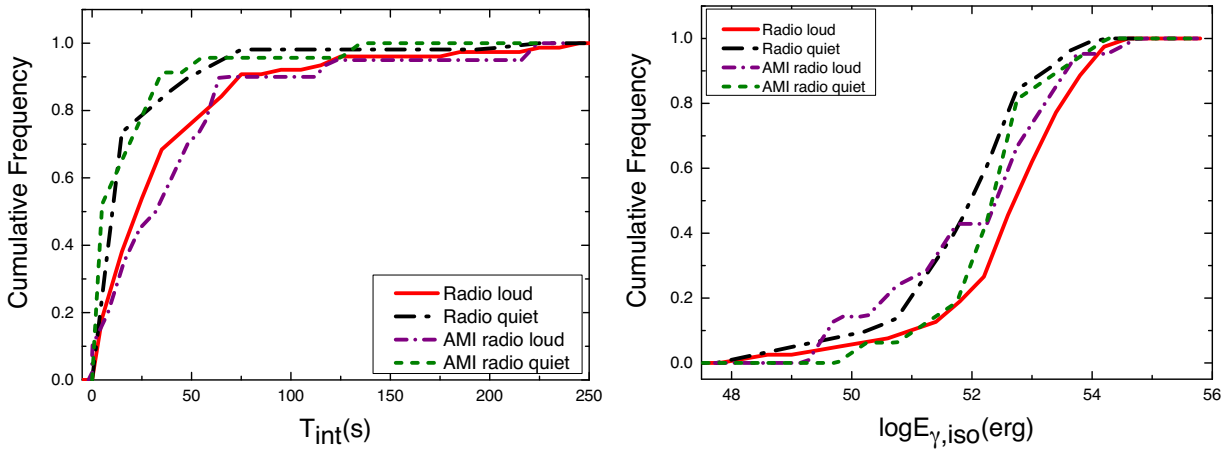

Figure 3. Cumulative fractions of $T_{\rm int}$ (left-hand panel) and $E_{\gamma,\,\rm iso}$ (right-hand panel) are plotted for the VLA-based radio-loud (red solid line), radio-quiet (blue dashed line) and for the AMI radio-loud (purple short dash–dotted line) and AMI radio-quiet (green short dashed line) GRBs.

Table 4. The relevant parameters of K-S tests.

Fig.[i]	N_1	N_2	D	P	$D_\alpha(N_1, N_2)$	Note[j]
1L	97[a]	112[b]	0.58	1.22×10^{-15}	0.18	Rejected
1R	45[a]	60[b]	0.56	5.8×10^{-8}	0.27	Rejected
2L	31[c]	46[d]	0.26	0.17	0.32	Accepted
2L	46[d]	54[e]	0.27	0.038	0.27	Rejected
2L	31[c]	54[e]	0.37	0.006	0.31	Rejected
2R	31[c]	43[d]	0.23	0.26	0.32	Accepted
2R	43[d]	51[e]	0.45	9.2×10^{-5}	0.28	Rejected
2R	31[c]	51[e]	0.32	0.03	0.31	Rejected
3L	77[f]	54[e]	0.31	0.003	0.24	Rejected
3L	21[g]	23[h]	0.35	0.11	0.41	Accepted
3R	74[f]	51[e]	0.37	3.2×10^{-4}	0.25	Rejected
3R	21[g]	16[h]	0.24	0.57	0.45	Accepted
4	25[f]	21[e]	0.31	0.19	0.40	Accepted
6	34[f]	15[e]	0.49	1.4×10^{-2}	0.45	Rejected
7L	79[f]	50[e]	0.37	2.1×10^{-4}	0.25	Rejected
7R	21[g]	23[h]	0.17	0.83	0.41	Accepted

Notes. N_1 and N_2 are two sample sizes. D is the K-S test statistic with a P value showing whether the two samples are taken from the same parent distribution. $D_\alpha(N_1, N_2)$ is the critical value in contrast with D for a significant level (SL) of $\alpha = 0.05$. The diverse samples characterized by whether the radio afterglows are detected or not are denoted by [a] for detection, [b] for upper limit, [c] for radio-loud I , [d] for radio-loud II, [e] for radio-quiet, [f] for radio-loud all, [g] for AMI radio-loud, and [h] for AMI radio-quiet.

[i] The capital letters represent the right-hand (R) and left-hand (L) panels in the corresponding figures.

[j] The bold face indicates those sample pairs with poor K-S test in a lower confidence level.

densities is extremely limited, we thus combine the radio-quiet and the radio-undetected samples into a newly formed radio faint sample in order to increase the statistical confidence level. Then, we plot the cumulative fractions for the two samples in Fig. 6 and apply a K-S test to get $D = 0.55$ with a probability of 0.002, which demonstrates that the radio-loud and radio faint samples are significantly incongruous with each other. In contrast, the medium densities of the radio-loud host galaxies are relatively larger than those of the radio faint ones. Furthermore, the fraction of low densities of $n \leq 0.1\,{\rm cm}^{-3}$ for the radio faint sample is around six times more than that for the radio-loud sample. On the contrary, about 90 per cent of radio-loud afterglows are surrounded by relatively denser mediums of $n \simeq 10^{-1} - 10^{2}\,{\rm cm}^{-3}$.

3.5 Spectral luminosity of radio afterglows

We utilize all the GRBs with measured isotropic γ-ray energy instead of $E_{\gamma,\rm iso} > 10^{52}$ (Lloyd-Ronning et al. 2019) only to ensure our samples to be as complete as possible. Simultaneously, we calculate the spectral peak luminosity at radio band ($L_{\nu,\,p}$) for the radio-loud and the radio-quiet (or upper limit) samples as (Zhang et al. 2018)

$$L_{\nu,\rm p} = 4\pi D_L^2 f_{m,\rm radio}(1+z)^{-1}k, \tag{3}$$

where $f_{m,\,\rm radio}$ denotes the peak flux density $F_{o,\,\rm peak}$ of the radio-loud afterglows or the upper limits of radio-quiet afterglows, k is a K-correction factor determined by

$$k = (1+z)^{\alpha-\beta}, \tag{4}$$

where $\alpha \sim 0$ and $\beta \sim 1/3$ are assumed to be the normal temporal and spectral indexes, respectively. Note that the spectral peak luminosity is proportional to the k factor and will evolve with the cosmological redshift in a different way if other set of α and β is assumed for a given burst. D_L denoting the luminosity distance of a burst is given by

$$D_L = cH_0^{-1}(1+z)\int_0^z {\rm d}z'[(1+z')^3\Omega_M + \Omega_\Lambda]^{-1/2}, \tag{5}$$

in which $c = 3.0 \times 10^8\,{\rm m\,s^{-1}}$ is the speed of light, H_0 is the Hubble constant taken as $70\,{\rm km\,s^{-1}\,Mpc^{-1}}$, other cosmological parameters $\Omega_M = 0.27$ and $\Omega_\Lambda = 0.73$ have been assumed for a flat universe

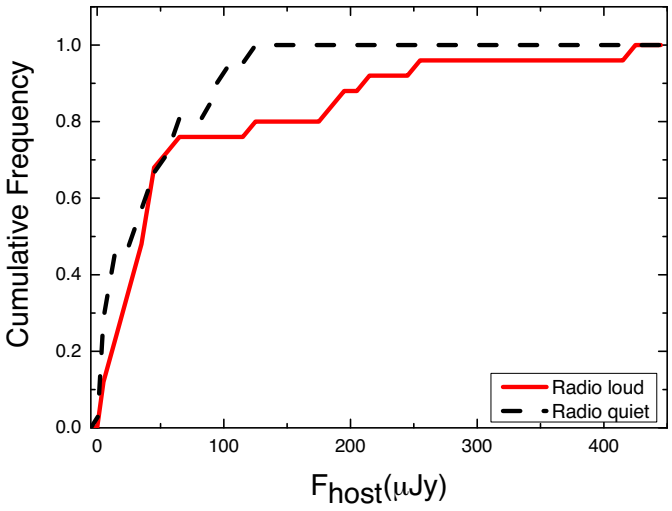

Figure 4. Cumulative fractions of $F_{\rm host}$ for radio-loud (solid red line) and radio-faint (black dashed line) samples.

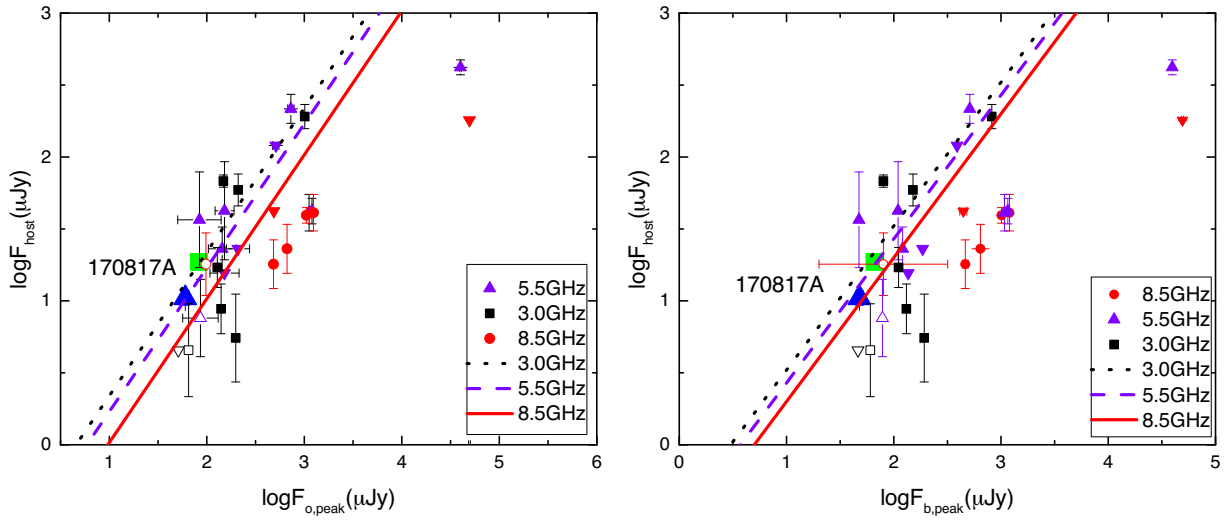

Figure 5. The relations of $F_{\rm host}$ versus $F_{o,\,\rm peak}$ and $F_{\rm host}$ versus $F_{b,\,\rm peak}$ are displayed on left- and right-hand panels, respectively, for different radio frequencies. Three correspondingly empirical power-low relations at frequencies of $\nu = 8.5$ GHz (solid line), 5.5 GHz (dashed line), and 3.0 GHz (dotted line) are compared. Those upper limits are marked with different downward arrows. The radio-loud and the radio-quiet bursts are denoted with filled and empty symbols, individually. The off-axis GRB 170817A is symbolized with large triangle for $\nu = 5$ GHz and large square for $\nu = 3$ GHz.

(Schaefer 2007). Consequently, the $L_{\nu,\,p}$ values can be obtained from equation (3) for the VLA-based GRBs at 8.5 GHz since most afterglows were detected at this frequency. For the AMI bursts reported in Anderson et al. (2018), their $L_{\nu,\,p}$ values are calculated at a frequency of 15.7 GHz. Owing to lack of measurement of the radio afterglows with the upper limits, the $L_{\nu,\,p}$ values of radio-quiet afterglows can be only estimated as the upper limits too. Fig. 7 displays the $L_{\nu,\,p}$ distributions of radio-loud, radio-quiet, and SN-associated GRBs, respectively. On average, the peak luminosity of radio-loud bursts is relatively larger than the other two, while the mean values of radio-quiet and SN-associated GRBs are comparable. The cumulative fractions of all the above samples are shown in Fig. 8. A K-S test to them shows that the luminosity distributions of radio-loud and radio-quiet GRBs are largely different for the VLA-based samples since $D = 0.37$ ($>D_{\alpha=0.05} = 0.25$) with $P \simeq 2.1 \times 10^{-4}$ and are however consistent with each other for the AMI samples. It needs to be emphasized that the distributional consistency of $L_{\nu,\,p}$ for different kinds of radio-selected GRBs is similar to that of the $E_{\gamma,\,\rm iso}$ distributions in Fig. 3. Moreover, the actual deviation between them would become more significant since the accumulative line of the radio-quiet sample consisted of the upper limits should move leftward in a certain sense. The median $L_{\nu,\,p}$ of radio-quiet sample is about one order of magnitude smaller than that of radio-loud sample. Interestingly, this is similar to the one order of magnitude difference between radio fluxes of host galaxies and GRB afterglows (Zhang et al. 2018). Hence, we conclude that the majority of radio-quiet emissions should be contributed by their surrounding host galaxies.

3.6 The $L_{\nu,\,p}$–$E_{\gamma,\,\rm iso}$ relationship

As shown in Figs 2, 3, 7, and 8, the averaged energies of $E_{\gamma,\,\rm iso}$ and $L_{\nu,\,p}$ of radio-loud bursts are larger than the corresponding values of radio-quiet ones. In the section, we will test the possible correlation between the $E_{\gamma,\,\rm iso}$ and the $L_{\nu,\,p}$ of radio-loud ($N = 100$) and radio-quiet ($N = 77$) GRB samples. For this purpose, the radio peak flux densities at 8.5 and 15.7 GHz have been utilized. Fig. 9 displays the relations of $E_{\gamma,\,\rm iso}$ with $L_{\nu,\,p}$ for all the radio-loud/quiet VLA-based bursts including 79 long GRBs (lGRBs), 19 SN/GRBs, 2 X-Ray

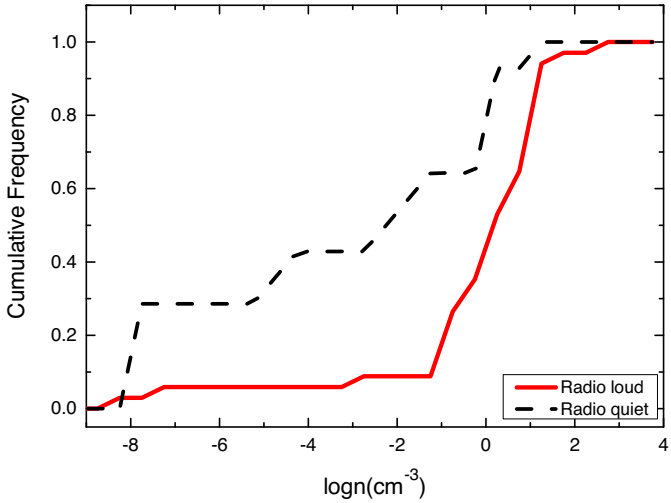

Figure 6. Cumulative fractions of log$n$ for radio-loud (red solid line) and radio faint (black dashed line) samples.

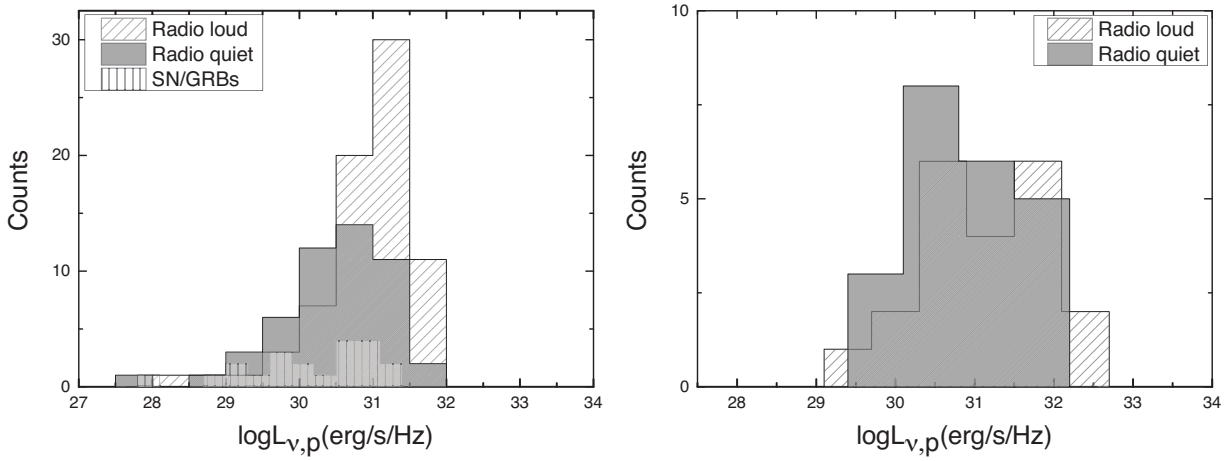

Figure 7. The left-hand panel shows the distribution of spectral peak luminosity of the VLA-based radio afterglows. The right-hand panel displays the distribution of spectral peak luminosity of the AMI GRBs. The filled and hatched histograms, respectively, represent the upper limit and detection samples, and the vertical-line hatched histogram corresponds to the SN/GRBs.

Flashes (XRFs), and one short GRBs (sGRBs), and 44 AMI GRBs. Interestingly, we find on the left-hand panel that $E_{\gamma,\,\rm iso}$ is positively correlated with $L_{\nu,\,p}$ with a Pearson correlation coefficient of $R = 0.76$ ($SL = 2.2 \times 10^{-16}$) or Spearman rank correlation coefficient of 0.55 ($SL = 1.08 \times 10^{-7}$). The correlation function can be roughly written as $L_{\nu,\,p} \propto E_{\gamma,\rm iso}^{0.41\pm0.04}$ for the whole radio-loud sample with $\chi_\nu^2 = 0.23$. On the right-hand panel, a positive correlation, $L_{\nu,\,p} \propto E_{\gamma,\rm iso}^{0.49\pm0.07}$ with a $\chi_\nu^2 = 0.42$, weakly exists for the radio-quiet bursts, of which the Pearson and the Spearman correlation coefficients are $R = 0.72$ ($SL = 5.48 \times 10^{-9}$) and $R = 0.61$($SL = 1.2 \times 10^{-6}$), respectively, that are very close to those of the radio-loud bursts. This demonstrates that the radio peak luminosities and the prompt γ-ray energies are highly associated. It is notable that our finding here is different from Chandra & Frail (2012), where they claimed no obvious correlation between $E_{\gamma,\,\rm iso}$ and $L_{\nu,\,p}$ in their fig. 20 possibly owing to the limit of sample size. Recently, Tang et al. (2019) found that the X-ray peak luminosity is positively correlated with the $E_{\gamma,\,\rm iso}$ as$L_X \propto E_{\gamma,\rm iso}^{0.97}$. It is valuable to mention that the radio peak luminosities of 21 SN/GRBs in our sample and six SN/GRBs in Chandra & Frail (2012) exhibit a consistent dependence of $E_{\gamma,\,\rm iso}$. This may imply these SN/GRBs should undergo with the same processes of energy dissipations. Data points of the sGRBs and the XRFs are too limited to show if they behave a positive interdependency as the lGRBs did.

3.7 The correlations between $T_{\rm int}$ and $1 + z$

Lloyd-Ronning et al. (2019) found that there was a negative correlation between $T_{\rm int}$ and $1 + z$ for the radio-loud rather than radio-quiet GRB sample. They concluded that if this negative correlation indeed exists, other than affected by the selection effect, it could reflect that the systems at higher redshift have less angular momentum or less materials accreted to the GRB discs. Recently, Zhang et al. (2018) investigated the correlations between the intrinsic peak times of radio afterglows at 8.5 GHz and the redshift factor $(1 + z)$ and found that they are fully uncorrelated, which seems to conflict with the negative correlation of $T_{\rm int}$ versus $1 + z$. Meanwhile, the $T_{\rm int}$ distribution of Swift/BAT bursts was still bimodal in that all the durations move towards to the short end once the T_{90} over $1 + z$ was considered (Zhang & Choi 2008). It is well known that the sGRBs are usually observed at nearby universe unlike the lGRBs. Strictly speaking, the negative dependence of the $T_{\rm int}$ on the redshift is hard to understand

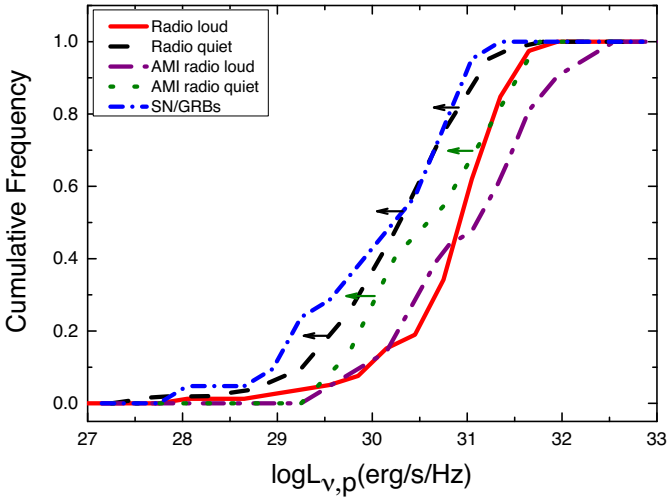

Figure 8. Cumulative fractions of $L_{\nu,p}$ for the VLA-based radio-loud (red solid line)and radio-quiet (black dashed line) samples, the AMI radio-loud (purple dash–dotted line), the AMI radio-quiet (green dotted line), and the SN-associated GRBs (blue short dash–dotted line). Note that the arrows denote that the $L_{\nu,p}$ distributions of radio-quiet GRBs are just the upper limits.

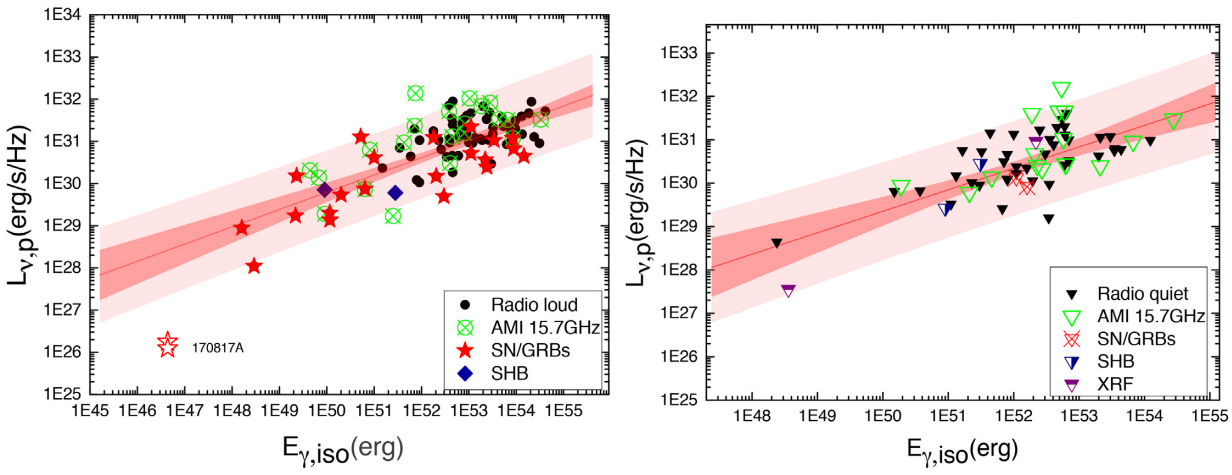

Figure 9. The correlations of $L_{\nu,p}$ versus $E_{\gamma,\rm iso}$ for radio-loud sample (the left-hand panel) and radio-quiet sample (the right-hand panel). All illustrations are marked on the insert. Note that the inverted triangles stand for the upper limits. Except the AMI radio-loud (cross circles) and radio-quiet (empty triangles) GRBs, all other symbols represent the VLA-based bursts. GRB 170817A detected at $\nu = 3$ and 5.5 GHz has been marked with two empty stars. The solid lines are the best power-law fits to all bursts but GRB 170817A. The light shaded regions are 2σ confidence ranges and the heavy shaded areas show the 2σ prediction ranges.

unless a fraction of sGRBs have extremely small redshift while parts of lGRBs have very high redshift.

As mentioned in Section 2, our current samples as an expansion of Lloyd-Ronning et al. (2019) are relatively complete. Therefore, it is timely and essential to check if the correlations between $T_{\rm int}$ and $1+z$ coexist in both radio-loud and radio-quiet samples as plotted in Fig. 10. In statistics, the Pearson correlations of $T_{\rm int}$ versus $1+z$ for the radio-loud and the radio-quiet samples give the R-indexes as –0.22 ($SL = 0.04$) and –0.20 ($SL = 0.18$) for the radio-loud and the radio-quiet lGRB samples, respectively. This demonstrates that the radio-loud GRBs do have a weaker negative correlation of $T_{\rm int}$ with redshift, of which this result is in good agreement with Lloyd-Ronning et al. (2019). Additionally, our radio-quiet sample also holds the similar anticorrelation with a 95.4 per cent confidence level like the radio-loud GRBs. We notice that the sGRBs in any case of our samples are outliers of the $T_{\rm int}$-$(1+z)$ correlation of the lGRBs and the sGRBs with smaller $T_{\rm int}$ and $1+z$ are systematically located at the bottom left-hand side of plane. Particularly, the radio-loud sGRB 170817A is situated within the transitional region between short and long GRBs. Hence, the $T_{\rm int}$ distributions of two kinds of GRBs are well in agreement with Zhang & Choi (2008).

4 CONCLUSION AND DISCUSSION

We carried out a systematic investigation of samples of radio-selected GRBs. Our main findings are as follows:

(i) According to the distributions of $T_{\rm int}$, $E_{\gamma,\rm iso}$, and $L_{\nu,p}$, we find that the radio-loud and the radio-quiet samples observationally differ with each other, particulary for the two energies $E_{\gamma,\rm iso}$ and $L_{\nu,p}$. Further divisions of radio-loud sample did not generate such significant distinctions.

(ii) It is also supported that the radio-loud and the radio-faint GRBs have largely different distributions of the surrounding medium densities, and could be thus originated from diverse central engines.

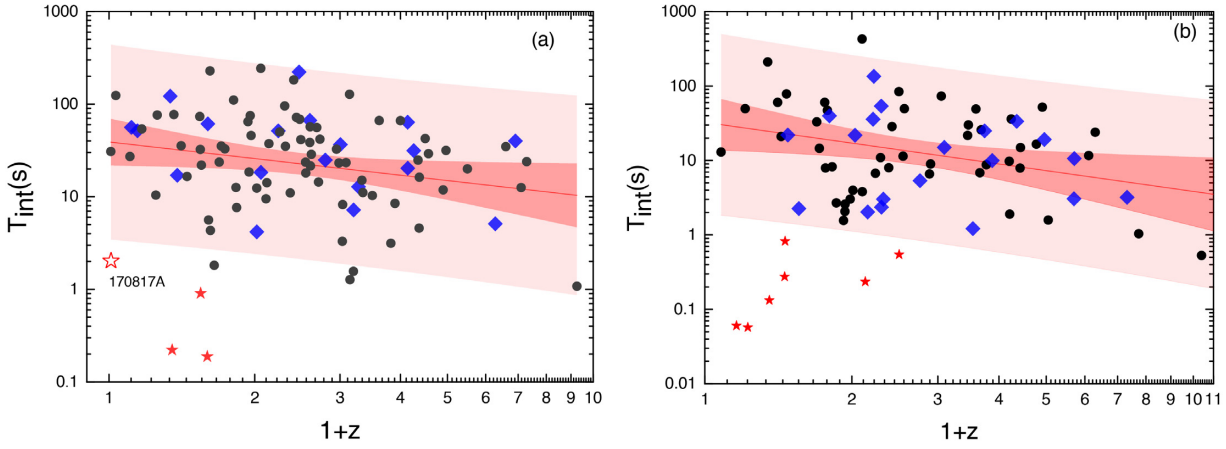

Figure 10. Panel (a) and (b), respectively, show the correlations between $T_{\rm int}$ and $1+z$ for the radio-loud and radio-quiet samples. The filled circles and diamonds denote lGRBs and the filled stars represent sGRBs. The red solid lines are the best fits to the observed data with a confidence level of 95.4 per cent (heavy shadow region) and a prediction of 2σ range (light shadow region). The AMI data at 15.7 GHz have been symbolized with blue diamonds. The radio-loud sGRB 170817A is characterized with an empty star in panel (a).

(iii) Although the radio flux density distributions of host galaxies for the radio-loud and the radio-faint samples are not significantly different, the flux densities of radio-quiet GRBs and their host galaxies are relatively lower than those of the radio-loud ones, which indicates the host types of both radio-loud and radio-faint GRBs might be diverse in essence.

(iv) The mean values of $F_{o,\,\rm peak}$, $T_{\rm int}$, $E_{\gamma,\,\rm iso}$, n, and $L_{\nu,\,p}$ for the radio-quiet GRBs are comparatively smaller than those of the radio-loud sample, correspondingly. However, the redshifts of two radio-selected samples are not found to be diversely distributed.

(v) Interestingly, we find $E_{\gamma,\,\rm iso}$ and $L_{\nu,\,p}$ are correlated with the power-law relations of $L_{\nu,\,p} \propto E_{\gamma,\,\rm iso}^{0.41\pm0.04}$ for the radio-loud sample and $L_{\nu,\,p} \propto E_{\gamma,\,\rm iso}^{0.49\pm0.07}$ for the radio-quiet sample, which were not distinguished by Chandra & Frail (2012) for the correlation between $E_{\gamma,\,\rm iso}$ and the peak radio spectral luminosity.

(vi) We follow Lloyd-Ronning et al. (2019) to study the dependencies of $T_{\rm int}$ with z for different radio-selected samples. Excitingly, we not only gain the anticorrelation between $T_{\rm int}$ and z for the radio-loud sample as Lloyd-Ronning et al. (2019) proposed, but also find that this dependency holds for the radio-quiet sample.

(vii) Despite of the AMI radio afterglows detected at higher frequency, almost all the above conclusions based on the VLA-based GRB samples are well supported.

Regarding the origin of the radio-undetected afterglows, it could result from several joint effects including the sensitivity of detectors (Chandra & Frail 2012), the contribution of host galaxies (Zhang et al. 2018), the extremely small energy outputs or the lower Lorentz factors of outflows (Zhang et al. 2015), etc. As predicted in our previous work by Zhang et al. (2015), the radio-undetected afterglows could be generated from those failed GRBs with normal energy outputs but much lower Lorentz factors (Huang, Dai & Lu 2002). Undoubtedly, the radio afterglows produced by one failed burst is undetectable for the former radio instruments. The Five-hundred-meter Aperture Spherical radio Telescope (FAST), as the largest single dish radio telescope in the world and a Chinese mega-science project (Nan et al. 2011; Li et al. 2018; Li, Dickey & Liu 2019; Jiang et al. 2020), had been successfully built in 2016 September and start formal operation nowadays. It is expected that these undetected radio afterglows, if existent physically, would become detectable in the near future. A FAST-centric VLBI network, which is being developed, will have unprecedented sensitivity, thus holds promise for revealing yet undetected radio afterglows. The Square Kilometre Array (SKA) will play an even more significant role in searching for such weak sources (Weltman et al. 2020).

Most of our radio-selected GRBs in the study are long bursts that are thought to be produced from core collapse of massive stars to form a black hole (Woosley 1993, MacFadyen & Woosley 1999). In the collapsar model, the intrinsic time $T_{\rm int}$ relies on the accretion rate that is related with the momentum of the progenitor system, namely larger momentum corresponds to longer $T_{\rm int}$, and the masses forming the accretion disc (Janiuk & Proga 2008). The collapsing progress exits in either a single stellar system or a binary system with three scenarios (Fryer, Woosley & Hartmann 1999), i.e. Scenario I: a single star evolves off main sequence and its winds blow off the hydrogen envelope to form a helium core, and then this helium core collapses to produce the GRBs; Scenario II: a binary system with primary evolving off main sequence evolves into a common envelope phase, and then after the H envelope was ejected the primary becomes a helium core collapsing and accreting the secondary to produce GRBs; Scenario III: this is also a binary system with primary evolving off main sequence into a common system, and then the secondary evolving off main sequence too, subsequently the system enter into a double-helium-star binary system. Finally, the two helium stars merge into one helium star and then the helium core collapse to cause the GRBs (Fryer et al. 1999). Because $T_{\rm int}$ is tightly determined by the momentum of collapsing systems, together with more masses accreted on the disc, Scenario I would readily lead to the longer $T_{\rm int}$ even though its angular momentum is expected to be less than the other two Scenarios (Fryer & Woosley 1998; Zhang & Fryer 2001).

Note that the soft lGRBs associated with core-collapse supernovae (Galama et al. 1998; Fryer et al. 1999; Woosley & MacFadyen 1999; Hjorth et al. 2003; Stanek et al. 2003; Campana et al. 2006; Xu et al. 2013) are generally believed to result from the deaths of massive stars. However, the hard sGRBs are usually thought to occur owing to the coalescence of two compact stars, such as double neutron stars, or a neutron star plus black hole system (Lee et al. 2007; Berger 2014). Therefore, the sGRBs with lower redshifts and isotropic γ-ray energies would be expected to have

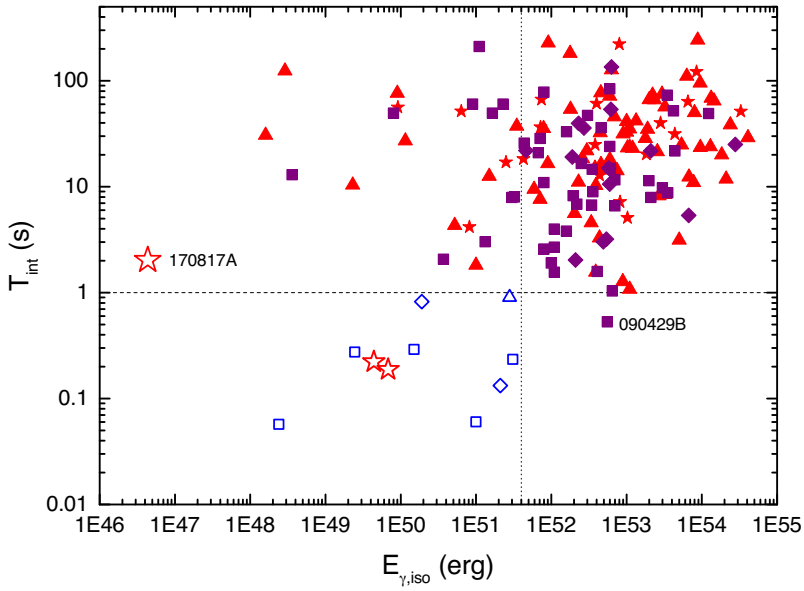

Figure 11. Relations of $T_{\rm int}$ with $E_{\gamma,\,\rm iso}$ for the radio-loud (triangles) and radio-quiet (squares) lGRB (filled symbols) and sGRB (empty symbols) in the VLA-based samples. Vertical and horizontal lines stand for $E_{\gamma,\,\rm iso} = 4 \times 10^{51}$ erg and $T_{\rm int} = 1$ s, correspondingly. The radio-loud and radio-quiet bursts in the AMI samples are identified with small stars and diamonds, respectively. sGRB 170817A is marked with a large star.

relatively shorter $T_{\rm int}$ in comparison with the lGRBs. We investigate the association of $E_{\gamma,\,\rm iso}$ with $T_{\rm int}$ in Fig. 11, from which we can see that there are no any correlations for either the sGRBs or the lGRBs. However, they can be separated by a horizontal line of $T_{\rm int} = 1$ s and a vertical line of $E_{\gamma,\,\rm iso} = 4 \times 10^{51}$ erg. All sGRBs but GRB 170817A possessing smaller $E_{\gamma,\,\rm iso}$ and $T_{\rm int}$ are located at the bottom left-hand corner. In comparison, the lGRBs with longer $T_{\rm int}$ relatively generate larger $E_{\gamma,\,\rm iso}$ spanning from $\sim 10^{48}$ to $\sim 10^{55}$ erg. Even though some lGRBs and sGRBs have comparable $E_{\gamma,\,\rm iso}$, their $T_{\rm int}$ values are completely distinct. It is valuable to focus on GRB 090429B, lying at the bottom right-hand corner, that is the farthest burst detected so far with $z \approx 9.4$ and $T_{90} = 5.5$ s (Cucchiara et al. 2011), whose progenitor is expected to be different from other lower redshift, especially short GRBs. Furthermore, we caution that sGRB 170817A differs from both the normal sGRBs and the low-energy lGRBs as depicted in Fig. 11. Very recently, Tang et al. (2019) found that the $E_{\gamma,\,\rm iso}$ and the T_{90} are positively correlated, and they explained that this might happen when the observed intensities of γ-rays were constrained within a certain range. We, nevertheless, find that the positive correlation trend disappears for the lGRBs in the rest frame. In principal, one may pursue to convert the observed $E_{\gamma,\,\rm iso}$ into the co-moving quantity by use of $E'_{\gamma,\,\rm iso} \simeq E_{\gamma,\,\rm iso}/\,\Gamma$, where Γ is the bulk Lorentz factor (Ghirlanda et al. 2012). Unfortunately, the Lorentz factor is still very hard to be determined precisely and uniquely although many authors have made great efforts (e.g. Sari & Piran 1999; Pe'er et al. 2007; Liang et al. 2010; Zou & piran 2010; Zou, Cheng & Wang 2015; Ghirlanda et al. 2018), which will be confirmed by further observations of the next-generation telescopes.

ACKNOWLEDGEMENTS

We thank the referee for very helpful comments and suggestion. This work is partly supported by the Ministry of Science and Technology of the People's Republic of China (2020SKA0120300), the Research Foundation of China (grant nos ZR2018MA030, XKJJC201901, and 201909118), the National Natural Science Foundation of China (grant nos U2031118, 11988101, 12041306, U1938201, 11873030, 11673023, U1838201, U1838202, U1838104, 11725313, and 11690024), the Strategic Priority Research Program of the Chinese Academy of Sciences ('Multiwaveband Gravitational Wave Universe', grant nos XDB23040000; XDA15360300), and the National Key Research and Development Program of China (2016YFA0400800, 2017YFA0402600). We thank Poonam Chandra for offering the data of GRB radio afterglows observed by VLA. We also acknowledge EW Liang, Nicole Lloyd-Ronning, LB Li, and HY Chang for helpful discussions.

DATA AVAILABILITY STATEMENT

The data underlying this article are available in the articles (Chandra & Frail 2012; Anderson et al. 2018) together with their online supplementary materials or in the archives on request, and the Gamma-ray Coordinates Network (GCN) at https://gcn.gsfc.nasa.gov/.

REFERENCES

Abbott B. P. et al., 2017, ApJ, 848, L13
Alexander K. D. et al., 2017, ApJ, 848, L21
Anderson G. E. et al., 2018, MNRAS, 473, 1512
Becerra R. L. et al., 2019, ApJ, 872, 118
Berger E., 2014, ARA&A, 52, 43
Berger E. et al., 2003, Nature, 426, 154
Berger E. et al., 2005, Nature, 438, 988
Bloom J. S., Frail D. A., Blustin A. J., Kulkarni S. R., 2003, ApJ, 594, 674
Campana S. et al., 2006, Nature, 442, 1008
Cenko S. B. et al., 2006, ApJ, 652, 490
Cenko S. B. et al., 2011, ApJ, 732, 29
Chandra P., Frail D. A, 2012, ApJ, 746, 156
Chandra P. et al., 2008, ApJ, 683, 924
Chandra P. et al., 2010, ApJ, 712, L31
Cucchiara A. et al., 2011, ApJ, 736, 7
Cusumano G. et al., 2007, A&A, 462, 73
de Ugarte Postigo A. et al., 2007, A&A, 462, L57
Duncan R. C., Thompson C., 1992, ApJ, 392, L9

Fong W., Berger E., Margutti R., Zauderer B. A., 2015, ApJ, 815, 102
Frail D. A., Waxman E., Kulkarni S. R., 2000, ApJ, 537, 191
Frail D. A. et al., 2003, ApJ, 590, 992
Frail D. A., Cameron P. B., Kasliwal M. et al., 2006, ApJ, 646, L99
Friedman A. S., Bloom J. S., 2005, ApJ, 627, 1
Fryer C. L, Woosley S. E., 1998, ApJ, 502, L9
Fryer C. L, Woosley S. E., Hartmann D. H., 1999, ApJ, 526, 152
Galama T. J. et al., 1998, Nature, 395, 670
Geng J. J et al., 2018, ApJ, 856, L33
Ghirlanda G. et al., 2012, MNRAS, 420, 483
Ghirlanda G. et al., 2018, A&A, 609, 112
Ghisellini G., Nardini M., Ghirlanda G., Celotti A., 2009, MNRAS, 393, 253
Goldstein A. et al., 2017, ApJ, 848, L14
Hancock P. J., Geansler B. M., Murphy T., 2013, ApJ, 776, 106
Hascoët R., Beloborodov A. M., Daigne F., Mochkovitch R., 2017, MNRAS, 472, L94
Hjorth J. et al., 2003, Nature, 423, 847
Huang Y. F., Dai Z. G., Lu T., 1999, A&A, 309, 513
Huang Y. F., Dai Z. G., Lu T., 2002, MNRAS, 332, 735
Huang Y. F., Gou L. J., Dai Z. G., Lu T., 2003, ApJ, 543, 90
Janiuk A., Proga D., 2008, ApJ, 675, 519
Jiang P. et al., 2020, RAA, 20, 64
Klebesadel R. W., Strong I. B., Olson R. A., 1973, ApJ, 182, L85
Kouveliotou C. et al., 1993, ApJ, 413, 101
Laskar T. et al., 2018, ApJ, 862, 94
Laskar T. et al., 2020, ApJ, 895, 64
Lee W. H., Ramirez-Ruiz E., 2007, New J. Phys., 9, 17
Li L. B. et al, 2015, MNRAS, 451, 1815
Li L. B. et al., 2018, ApJ, 880, 39
Li D. et al., 2018, IEEE Microw. Mag., 19, 112
Li D., Dickey J. M., Liu S., 2019, RAA, 19, 16
Liang E. W. et al., 2010, ApJ, 725, 2209
Lloyd-Ronning N. M., Fryer C. L., 2017, MNRAS, 467, 3413
Lloyd-Ronning N. M. et al., 2019, ApJ, 871, 118
MacFadyen A. I., Woosley S. E., 1999, ApJ, 524, 262
Mészáros P., 2006, RPPh, 69, 2259
Mu H. J et al., 2016, ApJ, 831, 111
Nan R. D. et al., 2011, IJMPD, 20, 989
Paczynski B., 1990, ApJ, 363, 218
Panaitescu A., Kumar P., 2002, ApJ, 571, 779
Pe'er A. et al., 2007, ApJ, 664, L1
Piran T., 1999, PhR, 314, 575
Rees M. J., Meszaros P., 1992, MNRAS, 258, 41
Rees M. J., Meszaros P., 1994, ApJ, 430, L93
Rhodes L. et al., 2020, MNRAS, 496, 3326
Sari R., Piran T., 1999, ApJ, 517, L109
Savchenko V. et al., 2017, ApJ, 848, L15
Schaefer B. E., 2007, ApJ, 660, 16
Schaefer B. E. et al., 2003, ApJ, 588, 387
Soderberg A. M. et al., 2004, Nature, 430, 648
Soderberg A. M. et al., 2006a, ApJ, 650, 261
Soderberg A. M. et al., 2006b, Nature, 442, 1014
Stanek K. Z. et al., 2003, ApJ, 591, L17
Tang C. H. et al., 2019, ApJS, 245, 1
Tashiro M. S et al., 2007, PASJ, 59, S361
Urata Y. J. et al., 2019, ApJ, 884, L58
Veres P. et al., 2015, ApJ, 810, 31
Weltman A. et al., 2020, PASA, 37, 2
Wijers R. A. M. J., Galama T. J., 1999, ApJ, 523, 177
Woosley S. E., 1993, ApJ, 405, 273
Woosley S. E., MacFadyen A. I., 1999, A&AS, 138, 499
Xu D. et al., 2013, ApJ, 776, 98
Zhang B., 2014, IJMPD, 23, 2
Zhang Z. B., Choi C. S., 2008, A&A, 484, 293
Zhang W., Fryer C. L., 2001, ApJ, 550, 357
Zhang Z. B. et al., 2015, RAA, 15, 237
Zhang Z. B., Chandra P., Huang Y. F., Li D., 2018, ApJ, 865, 82
Zou Y. C., piran T., 2010, MNRAS, 402, 1854
Zou Y. C., Cheng K. S., Wang F. Y., 2015, ApJ, 800, 23

APPENDIX A: COMPARISONS OF REDSHIFTS, TIME-SCALES, AND ENERGIES BETWEEN DIFFERENT RADIO-SELECTED GRBS

Here, we combine the VLA-based and the AMI GRBs to expand our sample and explore how the key parameters of the radio-selected GRBs with known redshift are distributed. In total, 100 radio-loud and 77 radio-quiet bursts have been included and compared in Fig. A1. Interestingly, the mean values of z, $T_{\rm int}$, and $E_{\gamma,\,\rm iso}$ become smaller and smaller and are ranked in order for radio-loud and radio-quiet GRBs. More importantly, this implies that radio-undetected GRBs with the lower γ-ray energy output and the shorter intrinsic duration time often occur in the nearby universe in contrast with other two kinds of GRBs with radio afterglows. However, only 24 per cent of radio-undetected sources belong to short GRBs, which hints that a significant fraction of long GRBs without any radio detections have lower values of $T_{\rm int}$ and $E_{\gamma,\,\rm iso}$. The new type of long GRBs is obviously different from most SN-associated GRBs with bright radio afterglow but lower $E_{\gamma,\,\rm iso}$ as shown in Fig. 9.

Comparing Figs 1, 7, and 9, one can obtain an interesting result that the median redshift of SN/GRBs is relatively lower than that of either radio-loud or radio-quiet GRBs. Recalling equation (3), we notice that the averaged peak flux density of SN/GRBs is comparable to (larger than) that of the radio-loud (radio-quiet) bursts, but the averaged spectral peak luminosities of SN/GRBs are relatively lower than the radio-loud GRBs and comparable to the radio-quiet bursts on a whole. It can be naturally interpreted by the fact that SN/GRBs are at relatively lower redshifts as compared with radio-loud and radio-quiet GRBs.

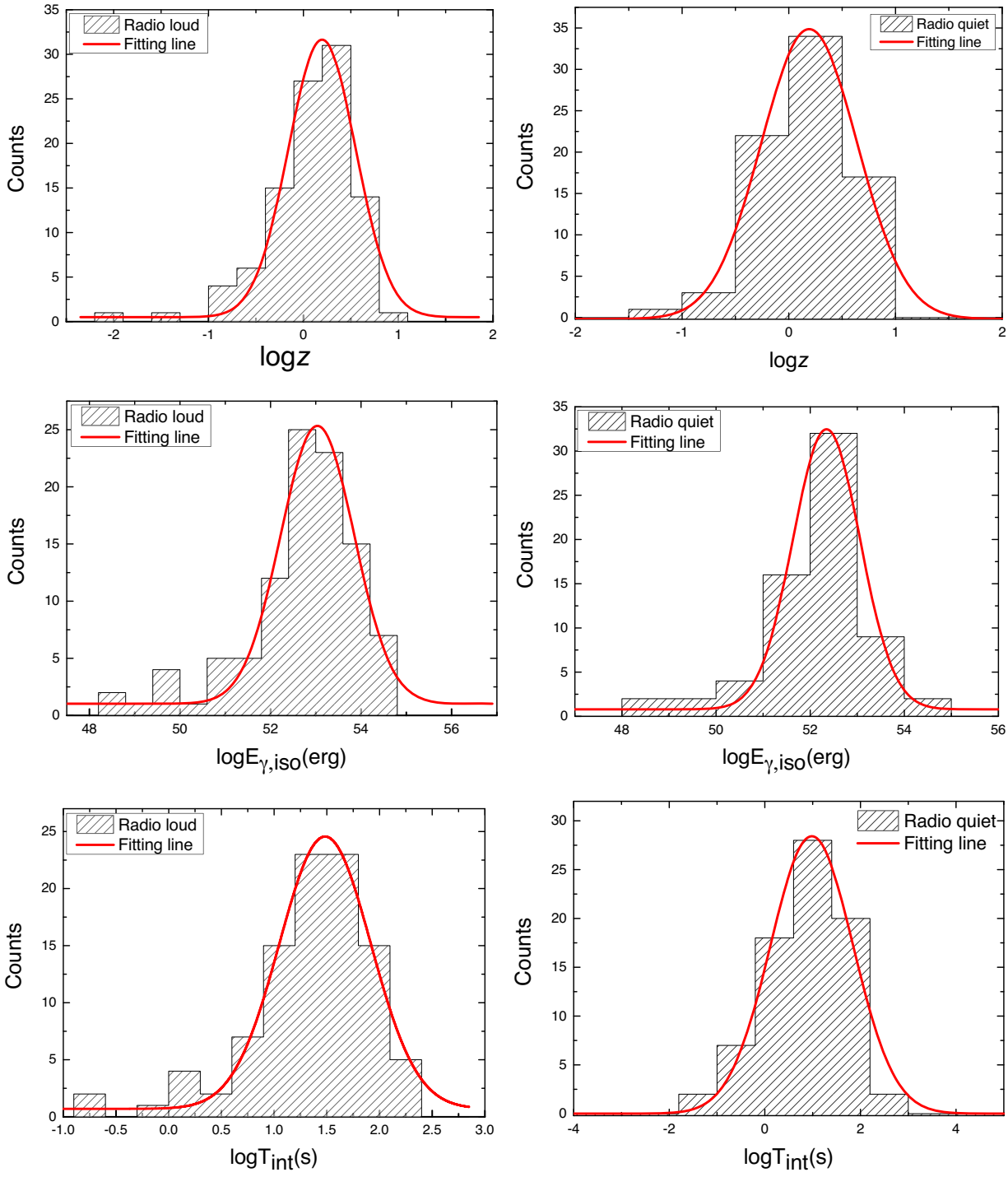

Figure A1. The histograms of z, $E_{\gamma,\,\mathrm{iso}}$, and T_{int} for the radio-loud and radio-quiet samples. The solid lines represent the best fit with a Gaussian function.

This paper has been typeset from a TEX/LATEX file prepared by the author.